IEEE Access
Multidisciplinary | Rapid Review | Open Access Journal

Received October 26, 2021, accepted November 10, 2021, date of publication November 12, 2021,
date of current version November 22, 2021.

Digital Object Identifier 10.1109/ACCESS.2021.3127941

Channel Modeling and Characterization for VLC-Based Medical Body Sensor Networks: Trends and Challenges

BARIS DONMEZ[1], (Member, IEEE), RANGEET MITRA[2], (Member, IEEE), AND FARSHAD MIRAMIRKHANI[1], (Member, IEEE)
[1]Department of Electrical and Electronics Engineering, Isik University, 34980 Istanbul, Turkey
[2]École de Technologie Supèrieure (ETS), Montreal, QC H3C 1K3, Canada

Corresponding author: Farshad Miramirkhani (farshad.miramirkhani@isikun.edu.tr)

This work was supported by the Scientific Research Projects (BAP) under Grant 20A204.

ABSTRACT Optical Wireless Communication (OWC) refers to transmission in unguided propagation media through the use of optical carriers, i.e., visible, Infrared (IR), and Ultraviolet (UV) bands. In this paper, we focus on indoor Visible Light Communication (VLC)-based Medical Body Sensor Networks (MBSNs) which allow the Light Emitting Diodes (LEDs) to communicate between on-body sensors/subdermal implants and on-body central hubs/monitoring devices while also serving as a luminaire. Since the Quality-of-Service (QoS) of the communication systems depends heavily on realistic channel modeling and characterization, this paper aims at presenting an up-to-date survey of works on channel modeling activities for MBSNs. The first part reviews existing IR-based MBSNs channel models based on which VLC channel models are derived. The second part of this review provides details on existing VLC-based MBSNs channel models according to the mobility of the MBSNs on the patient's body. We also present a realistic channel modeling approach called site-specific ray tracing that considers the skin tissue for the MBSNs channel modeling for realistic hospital scenarios.

INDEX TERMS Channel modeling, medical body sensor networks (MBSNs), optical communication, transdermal communication (TC), visible light communication (VLC).

I. INTRODUCTION

Optical Wireless Communication (OWC) has emerged as a promising technology for 6G and beyond communication networks. The optical transmission allows for spatial re-utilization and protection from Radio Frequency (RF) co-channel and inter-symbol interference, and thus is an attractive solution for addressing the existing spectrum crunch in wireless communication. The primary benefits of OWC include ultra-high bandwidth over an unregulated license-free spectrum, ultra-high data rate, and ultra-low latency [1]–[4]. Among several OWC methods, Visible Light Communication (VLC) refers to signaling within a sub-spectrum of optical spectrum (79 to 430 THz) that is potentially useful for wireless transmission using fast-switching Light-Emitting Diodes (LEDs) in accordance with the input messages. Therefore, for the VLC systems, the LEDs are known to function dually as both optical-transmitters and luminaries.

VLC transcends the traditional RF based systems due to the properties of its physical layer. Firstly, VLC provides a secure communication since the light rays cannot pass through opaque materials. This makes VLC an ideal supplement for RF based systems for indoor applications, such as, Medical Body Sensor Networks (MBSNs) [1]–[7]. In this regard, the IEC 60601-1-2 standard for VLC MBSN are found to allow for a minimal distance between a medical equipment and RF transceiver to prevent deterioration in the Quality-of-Service (QoS) [8]. In addition, VLC is known to have a large bandwidth. Furthermore, VLC is unlicensed, which makes its case as an auxiliary technology that potentially eases the typically heavy data traffic in an indoor environment [9].

With intensification of research-activities in VLC, recent surveys review various aspects of VLC. In [3],

The associate editor coordinating the review of this manuscript and approving it for publication was Luca Barletta.

a comprehensive survey on VLC was provided with an emphasis on challenges such as bandwidth enhancement, interference and noise removal, non-linearity compensation and signal clipping, and optical beamforming faced in indoor applications over the period of 1979-2014. In [10], another survey covered physical layer issues, medium access techniques, system design and programmable platforms, and Visible Light (VL) sensing for indoor applications. In [11], VLC-based Indoor Positioning Systems (IPS) are classified according to an accuracy-analysis of VLC-based-IPS in experimental and simulation environments. In [12], a survey of channel modeling for indoor VLC was published covering five different types of typical indoor VLC channel models with their pros and cons together with their application scenarios. In [13], a survey of OWC channel measurement campaigns and channel models covering indoor, outdoor, underground, and underwater environments was presented. In the existing VLC literature, there are several other papers which address the challenges that could potentially enhance VLC system design and align it with consumer-challenges [14]–[16].

In the current decade, OWC-based MBSNs have attracted increased attention in recent works. In details, the Infrared (IR) communication has already been used in hospitals for tetherless communication between body sensors and monitoring equipment. In this regard, some standards has been also established for the mobile IR devices placed next to the patient in static Line-of-Sight (LoS) configurations [17]. On the other hand, when designing an OWC system, the IR transmitters and non-coherent light sources such as LEDs must conform to eye safety standards [18], [19]. In [20], common challenges of the wireless MBSNs system were reviewed. For example, energy efficiency was discussed as a significant challenge since the wireless communication is the most power consuming part of the MBSNs. Further, the presence of body in the system degrades the channel performance, and hence modeling realistic channels which consider the complex body structure, and its movement were also introduced as one of the key challenges. It should be especially noted that [20] focused on the general overview rather than the comprehensive channel modeling. Besides, the existing wireless MBSNs communication systems in literature are based on the RF, acoustic, and long wave magnetic signals which is subjected to IEEE 1902.1.

Despite the increased attention on OWC-based MBSNs, there is a lack of relevant channel models that are specifically applicable to the OWC-based MBSNs. This lacuna of accurate channel-models is indeed a serious concern since channel modeling is the very first step for efficient, reliable, and robust link design/link enhancement. Existing deterministic [21]–[28] and stochastic [29]–[32] IR channel models are utilized for the modeling of uplink channels, while deterministic [33]–[40] and stochastic [41]–[47] VLC channel models are advantageous for modeling downlink channels in OWC-based MBSNs.

Since IR channel models have already laid the groundwork for VLC channel models, this paper starts with an overview of uplink IR MBSNs channel modeling [48]–[58]. Both deterministic recursive method [48]–[52] and stochastic Monte Carlo Ray Tracing (MCRT) models [54]–[58] are utilized to obtain IR channel models. Earlier studies on IR-based MBSNs mostly focused on simplistic scenarios where an ideal Lambertian source is considered, and the effects of photodetector carrying body and room equipment are neglected [48]–[52]. In [50], a simple dynamic LoS channel was modeled. Further, in [52], an uplink Multiple-Input Multiple-Output (MISO) IR channel model was established using Zero Cross Correlation (ZCC)-based Optical Code-Division Multiple-Access (OCDMA). In [53], for an alternative modulation scheme namely, the Non-Return-to-Zero-Alternate Mark Inversion (NRZ-AMI), experimental validation was presented for its improved performance compared to conventional NRZ-On Off Keying (OOK) against the IR light interference. The multiple access uplink IR scenarios were considered as Single-Input Multiple-Output (SIMO) IR scheme in [54]–[58]. The shadowing effect of the transmitter carrying body was considered in [57] and [58].

It should be noted that the IR transmitters operate on a single optical frequency whereas the common white VL source is inherently polychromatic. Since the reflectance of most materials vary according to the wavelength of reflected signals, VLC channel models that use polychromatic light sources are much more complex than the corresponding IR channels. In this context, the IR channel models cannot be adopted in a straightforward manner for VLC channel modeling.

Earlier studies on VLC-based MBSNs [59]–[65] mostly focused on idealistic scenarios where fixed Lambertian reflectance is considered, and the photodetector carrying body and room equipment are neglected [59], [60]. An experimental model for the simplest LoS channel was derived in [59]. Further, body presence modeling in 2D and 3D was presented in [61]. In [62], room equipment and fixed non-Lambertian reflectance were considered. The multiple access downlink VLC scenarios were considered as MISO scheme in [60]–[62]. Moreover, [64] considered SIMO IR scheme and MISO VLC scheme together. Furthermore, the impact of shadowing on both links, and power optimization at required QoS were investigated in [65].

Against this background, we present a comprehensive survey on optical wireless MBSNs channel modeling from past to present by reviewing the existing works and highlighting the key points and challenges. The rest of the paper is organized as follows: Section II reviews the existing IR-based MBSNs channel models. Section III presents the VLC-based MBSNs channel models that build upon earlier IR-based ones and discusses the static and mobile channel models. Section IV presents the site-specific MBSNs channel modeling where the optical characterization of human skin, channel modeling methodology, and channel characterization

of various MBSN scenarios have been detailed. The future research directions for VLC-based MBSN channel modeling are outlined in Section V. Finally, conclusions are drawn in Section VI.

II. IR-BASED MBSNs CHANNEL MODELS

In previous section, we introduced OWC-based MBSNs technology. In this section, we overview the existing IR-based MBSNs channel models [48]–[58] which are modelled by the deterministic recursive method [48]–[52], or by stochastic MCRT approach [54]–[58]. These models are summarized in Table 1. It is also worth mentioning that the optical channels are characterized by optical channel DC gain H_0 and temporal time dispersion of the channel τ_0. However, the narrowband flat fading channels with low data rates (i.e., lower than 10 Mbps) [65] and high QoS (i.e., low outage probability) [66] are established for MBSNs applications where the effect of Inter Symbol Interference (ISI) is negligible. Therefore, the optical channel models for MBSNs can be characterized by the statistical distribution of channel DC gain [2].

In [48], the diffuse IR wireless channel for a mobile patient whose mobility was statistically modelled in 2D and 3D inside a room with dimensions of 3 m × 4 m × 2.5 m is modelled by using deterministic recursive approach [22]. In this approach, the multiple reflection Channel Impulse Response (CIR) was obtained through two sequential stages. In the first stage, the reflective surfaces are assumed as purely Lambertian surfaces and then discretized into tiny surface elements. Each tiny reflecting element with an area dA and reflectivity ρ is considered as a receiver with an area dA and received power dP. In the next stage, each of these tiny receivers is considered as a power source and the total received power at the Photodetector (PD) is then computed by collecting the contributions of each of these reflective elements. In this approach, the CIR of a single ray with an arbitrary number of reflections is computed recursively and then, the overall CIR is obtained by the summation of CIRs of each ray emitted from the light source. The light source $S = \{\mathbf{r}_S, \hat{\mathbf{n}}_S, m\}$ is described with three parameters, i.e., the arbitrary source position $\mathbf{r}_S$, source orientation $\hat{\mathbf{n}}_S$, and the Lambertian order of m. Moreover, the receiver $R = \{\mathbf{r}_R, \hat{\mathbf{n}}_R, A_R, FOV\}$ is described by four parameters, i.e., the arbitrary position of the receiver $\mathbf{r}_R$, receiver orientation $\hat{\mathbf{n}}_R$, detector area A_R, and the field of view FOV. The multiple bounce CIR therefore can be obtained as (1), as shown at the bottom of the page, where k is the reflection order; N is the total number of reflective elements; ε_i is the i^{th} reflective element; ρ_i is the reflectivity of i^{th} reflective element; α is the irradiance angle; β is the incident angle; d is the distance between the source and the receiver; c is the speed of light; and ΔA is the area of reflective element. Besides, $\hat{\mathbf{n}}$ denotes the normal to the surface at location $\mathbf{r}$, $\otimes$ indicates the convolution, and rect(ξ) is defined as

$$\text{rect}(\xi) = \begin{cases} 0 & |\xi| > 1, \\ 1 & |\xi| \leq 1. \end{cases} \tag{2}$$

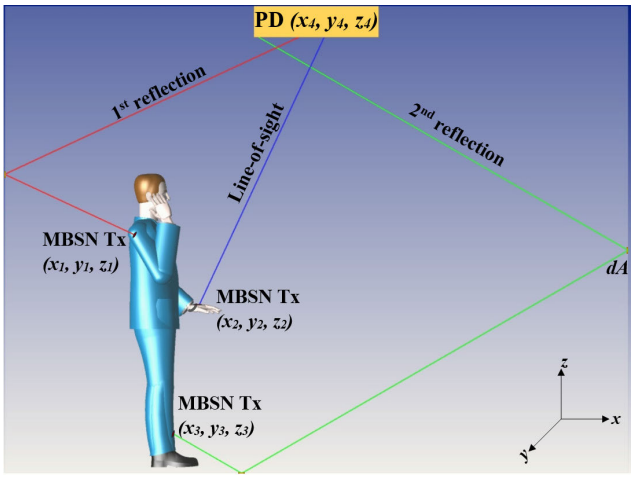

FIGURE 1. Recursive approach for MBSNs channel modeling.

Tracing of a single ray in deterministic recursive approach is shown in Fig. 1. Although this recursive method allows obtaining the overall CIR for multiple bounce for any order, if $k > 3$ the computation duration and computer memory requirements will increase drastically. For this reason, first order reflection from floor was considered in [48]. Besides, the scenario in [48] was built upon some simplifying assumptions such as empty room, purely Lambertian reflection, fixed reflectance values and ideal Lambertian source.

In [49], both LoS and Non-Line-of-Sight (NLoS) IR wireless channels were modelled by recursive method for a mobile patient whose 3D location was modelled by Gaussian distribution inside a room with dimensions of 3 m × 4 m × 2.5 m. The scenario in [49] was built upon some simplifying assumptions such as empty room, purely Lambertian reflection, fixed reflectance values and ideal Lambertian source.

In [50], LoS IR wireless channel was modelled by recursive method for a mobile patient whose location was modelled in both 2D and 3D by uniform and Gaussian distributions inside a room with dimensions of 3 m × 4 m × 2.5 m. Assuming perfect alignment between transmitter and receiver, the Probability Density Function (PDF) of channel gain, achievable data rate R_b, and minimum possible transmission power P

$$h^{(k)}(t; S, R) \approx \sum_{i=1}^{N} h^{(0)}(t; S, \varepsilon_i) \otimes h^{(k-1)}(t; \varepsilon_i, R) = \frac{m+1}{2\pi} \sum_{i=1}^{N} \frac{\rho_i \cos^n(\alpha) \cos(\beta)}{d^2} \, rect\left(\frac{2\beta}{\pi}\right) h^{(k-1)}\left(\frac{t - d_i}{c}; \{r, \hat{n}, 1\}, R\right) \Delta A \tag{1}$$

TABLE 1. Comparison table of studies on uplink IR-based MBSNs channel models.

	Method	Modeling of Reflectance	Number of Reflections	Other Assumptions	Configuration under Consideration
[48]	Recursive algorithm	Fixed reflectance	First order	-Purely Lambertian -Empty room -Ideal Lambertian source	There is a mobile patient whose mobility was statistically modelled in 2D and 3D inside a room with dimensions of 3 m × 4 m × 2.5 m.
[49]	Recursive algorithm	Fixed reflectance	First order	-Purely Lambertian -Empty room -Ideal Lambertian source	Both LoS and diffuse infrared wireless channels were modelled for a mobile patient whose 3D location was modelled by Gaussian distribution inside a room with dimensions of 3 m × 4 m × 2.5 m.
[50]	Recursive algorithm	N/A (LoS)	No reflection	-Empty room -Ideal Lambertian source	A mobile patient whose location was modelled in both 2D and 3D by uniform and Gaussian distributions inside a room with dimensions of 3 m × 4 m × 2.5 m was considered.
[51]	Recursive algorithm	Fixed reflectance	First order	-Purely Lambertian -Empty room -Ideal Lambertian source	LoS with perfect alignment and misalignment, and diffuse infrared wireless links were considered for a mobile patient whose location was modelled by Gaussian distribution inside an empty room with dimensions of 3 m × 4 m × 2.5 m.
[52]	Recursive algorithm	Fixed reflectance	First order	-Purely Lambertian -Empty room -Ideal Lambertian source -MISO IR scheme	LoS and NLoS infrared wireless links were considered for a patient with 2D and 3D mobility in an empty room with dimensions of 4 m × 4 m × 3m.
[53]	Experiment	Fixed reflectance	First order	-Purely Lambertian -Empty room -Non-ideal Lambertian source	The realistic ambient light interference was considered for a mobile diffuse infrared channel inside an empty room with dimensions of 3 m × 3 m × 3 m.
[54]	Monte Carlo ray tracing algorithm	Fixed reflectance	Third order	-Purely Lambertian -Empty room -Non-ideal Lambertian source -SIMO IR scheme	MCRT simulations assuming third order reflections were verified with experimental results for an empty room with dimensions of 6.6 m × 6.7 m × 3 m.
[55]	Monte Carlo ray tracing algorithm	Fixed reflectance	Third order	-Purely Lambertian -Empty room -Non-ideal Lambertian source -SIMO IR scheme	MCRT simulations assuming third order reflections were verified with experimental results for an empty room with dimensions of 6.6 m × 6.7 m × 2.5 m.
[56]	Monte Carlo ray tracing algorithm	Fixed reflectance	Third order	-Purely Lambertian -Empty room -Non-ideal Lambertian source -SIMO IR scheme	An uplink IR with third order reflections was considered for an empty room with dimensions of 6.7 m × 6.6 m × 3 m. The receiver was considered with orientation angles of 5°, 10°, 15°, 20°, 25°, 30°, 45°, 60°, 75°, 90° while the optical transmitter had directivities of $m = 1$, 2, 3, 5, 7, 11, 45.
[57]	Monte Carlo ray tracing algorithm	Fixed reflectance	Third order	-Purely Lambertian -Empty room -Non-ideal Lambertian source -3D human body and robotic platform models -SIMO IR scheme	MCRT simulations assuming third order reflections were verified with experimental results for an empty room with dimensions of 6.6 m × 6.7 m × 3 m. Various transmitter heights of $h = 0.15$, 0.22, 0.5, 0.9, 1.2, 1.5, and 1.7 m in the absence and presence of human body were also considered.
[58]	Monte Carlo ray tracing algorithm	Fixed reflectance	Third order	-Purely Lambertian -Empty room -Ideal Lambertian source -3D human body model -SIMO IR scheme	MCRT with third order reflections were simulated for an empty room with dimensions of 6.6 m × 6.7 m × 3 m. Various gaits corresponding to a young person and a humpbacked old person are considered in the random walk model.

were obtained. The results in [50] revealed that more precise channel models can be obtained where the location is modelled in 2D by Gaussian distribution. The scenario in this work was built upon some simplifying assumptions such as empty room, purely Lambertian reflection, fixed reflectance values and ideal Lambertian source.

In [51], LoS with perfect alignment and misalignment, and diffuse IR wireless channels were modelled by recursive method for a mobile patient whose location was modelled in both 2D and 3D by uniform and Gaussian distributions inside a room with dimensions of 3 m × 4 m × 2.5 m. The scenario in this work was built upon some simplifying assumptions such as empty room, purely Lambertian reflection, fixed reflectance values and ideal Lambertian source. The PDF of channel gain for these three different configurations was obtained and it was observed that the highest channel gain appears in LoS with perfect alignment scheme as expected. It was also observed that in the misaligned LoS and diffuse links the corresponding curves shift in the direction of lower channel gain values due to loss of some reflected rays which degrades the received power. The results in [51] also revealed that the misalignment angle range must be restricted within [0°, 30°] to ensure desired QoS levels while this would restrict the possible mobility scenarios.

In [52], LoS and single bounce NLoS IR wireless channels were modelled by recursive method for a patient with 2D and 3D mobility in an empty room with dimensions of 4 m × 4 m × 3 m. The scenario in this work built

upon some simplifying assumptions such as empty room, purely Lambertian reflection, fixed reflectance values and ideal Lambertian source. Multiple medical sensors coupled with transmitters on patient's body were considered where each node communicates with PD on the ceiling as uplinks. OptiSystem® software was utilized to compute the received power whereas Matlab® was used to model the channel and patient mobility. The PDF of channel gain for both 2D and 3D mobility in LoS and single bounce channels were obtained and the results showed that the NLoS channel is more spread than that of LoS. The maximum possible number of medical nodes was also investigated by differentiating these nodes with OCDMA based on ZCC code, for a given QoS.

The work in [53] presented experimentally the mitigation of ambient light interference on a mobile diffuse IR channel. A low-cost commercial IR-LED at 850 nm with a power of 350 mW was used as a transmitter in a laboratory environment with dimensions 3 m × 3 m × 3 m. The receiver was fixed on the ceiling centre and the location of the transmitter on the body was modelled randomly in 2D with a fixed height of 1.4 m. A surface with a fixed Lambertian reflectivity of 0.7 was placed 1.4 m further from the transmitter which can be considered as a single floor bounce model. The detector was also placed 3 m further from the same reflective surface where 25 equally distributed transmitter locations on the 3 m × 3 m floor area were also considered. The authors then proposed a DC balanced bipolar coding, i.e., NRZ-AMI line coding, to overcome the noise and significant improvements in the BER performance were reported using the channel models.

In [54], a ray tracing channel simulator was proposed which accounts for the transmitter/receiver position, orientation, directivity, Field of View (FOV) and surface area as the IR channel modeling components. The simulation results were also verified by experiments. In the experimental setup, a triaxial accelerometer was integrated into a wearable device on patient's arm. A high-power IR diode (TSAL5100) at 940 nm was chosen as the transmitter and four receivers with FOV of 45° were fixed on the ceiling of a furnished room with dimensions of 6.6 m × 6.7 m × 3 m. The experimental results indicated that the packet loss decreases while the number of receivers increases.

In [55], MCRT simulations that consider third order reflections were verified with experimental results. In the simulations, the location of mobile patient wearing the transmitter on the arm was modelled by uniform distribution. In the experimental setup, a wearable accelerometer-based device was placed on the patient's arm. TSAL5100 and TSAL7600 optical transmitters with half power angles $\varphi_{1/2} = 10°$ and $\varphi_{1/2} = 30°$, respectively, were considered as transmitter and four identical IR receivers were fixed on the ceiling of a room with dimensions of 6.6 m × 6.7 m × 2.5 m. The PDF of channel gain was then obtained for single active receiver scenario at $\varphi_{1/2} = 10°$ and $\varphi_{1/2} = 30°$. Both experimental packet loss values and theoretical PDF of channel gain showed that IR transmitter with $\varphi_{1/2} = 30°$ outperforms that with $\varphi_{1/2} = 10°$. It was also observed that the packet loss decreases while the number of active receivers increases.

In [56], an uplink IR communication between a transmitter located on the mobile patient and fixed four receivers with various orientations located on the ceiling of an empty room with dimension of 6.7 m × 6.6 m × 3 m was investigated. Uniformly distributed transmitter locations were considered with 10^4 points, with 10^4 links for each receiver. The Switching Combining (SwC) technique was also utilized for diversity. The CDF of channel gain for double, triple, and quadruple active receivers with orientation angles of 45° and 90° were presented. The results revealed that increasing number of the receivers with an orientation angle 45° improves the channel performance. It was also observed that the panel receivers oriented at 45° offer a better channel performance than the perpendicular oriented one because the former one can collect more reflected lights. An experiment was also presented for the same room for validation of the theoretical results. The experimental results showed that for receivers with parallel orientation, a diffused transmitter would establish a channel with higher reliability. On the other hand, if the panel receivers are perpendicularly oriented, then a collimated transmitter is a better option for modeling a channel with higher bandwidth due to the minimization of collected rays with high-order reflections.

In [57], MCRT simulations with third order reflections were verified with experimental results for an empty room with dimensions of 6.7 m × 6.6 m × 3 m. A rectangular-shaped human body as well as a robotic platform in 3D with a fixed Lambertian reflectance value were modelled to address the body impact on realistic channel modeling. Four active receivers with 45° orientation were located at the corners of the square panel lighting that is fixed on the ceiling center. The patient location was also distributed uniformly among 10^4 points on 2D plane. The CDF of channel gain for various transmitter heights of $h = 0.15$, 0.22, 0.5, 0.9, 1.2, 1.5, and 1.7 m were presented in the absence and presence of the human body. The results in [57] revealed that the channel performance degrades significantly when the transmitter height is less than 1.2 m due to the blockage of the human body.

In [58], an uplink IR communication between a randomly orienting transmitter located on the mobile patient's wrist and fixed four receivers with 45° orientation placed on the ceiling in an empty room with a dimension of 6.7 m × 6.6 m × 3 m was investigated. Different gait patterns corresponding to a young person and an old person are considered in the random walk (RW) model. The Lambertian reflectivity of the room surfaces and 3D human bodies are considered as 0.8 and 0.1, respectively. A Lambertian source is taken into consideration in MCRT simulations with three reflections. According to the simulation results, the channel gain is overestimated if the simulation results of a young person who walks upright are considered rather than those of a humpbacked older person when designing an IR-based MBSNs system for an elder.

However, selecting any of these bodies leads to an insignificant impact on the channel selectivity.

While earlier works in [48]–[58] discussed uplink IR-based MBSNs channel models, there are some works on node-to-node (i.e., on-body) MBSNs channel models [67]–[71]. In [67] and [68], a static on-body IR-based MBSNs channel models were investigated. In [67], stochastic MCRT method was used whereas deterministic single bounce recursive method was adopted in [68]. Idealistic assumptions such as ideal Lambertian source and fixed reflectance values were considered in these works and ideal wavelength-independent sources were considered. In [69], deterministic one bounce recursive model was adapted to model a mobile on-body IR channel in a diffuse configuration. In [70], a mobile on-body IR channel with MISO scheme was modelled in a diffuse configuration where the differentiation between the signals of each transmitter nodes was established by utilizing unipolar Optical Orthogonal Code (OOC)-based OCDMA. In [71], a mobile on-body IR channel was modelled in a diffuse configuration. Ten on-body sensors coupled with transmitters communicate with two coordinator nodes coupled with receivers placed on the hip and the shoulder while 3D body moves in a realistic walk cycle. The non-sequential MCRT algorithm with $k = 3$ was adopted which allows to create realistic environment. Patient random mobility was also modelled with modified Random Waypoint (RWP) model. The optical channel DC gain, Root Mean Square (RMS) delay spread, and coherence time features were obtained to characterize the channels between the transmitter sensor nodes and receiver coordinator nodes in local and global mobility scenarios.

III. VLC-BASED MBSNs CHANNEL MODELS

In Section II, the existing IR-based MBSNs channel models are discussed [48]–[58]. In this section, we overview the existing VLC-based MBSNs channel models [59]–[65] which are summarized in Table 2. In terms of the mobility of the corresponding transmission component, these works can be categorized into static and dynamic channel models. It should be noted that both unidirectional and bidirectional communication modes have been considered in existing dynamic channels.

A. STATIC CHANNEL MODELS

In [59], the static LoS downlink VLC channel was experimentally established where the location of the transmitter and receiver are fixed with LoS distance 0.5 m. The NRZ-OOK modulation was used with a carrier frequency of 100 kHz to not disturb the human eye while both illuminating and transmitting data. The results showed that a maximum data rate of 56 kbps is achieved for targeted $BER = 10^{-6}$.

In [72]–[75], the static LoS uplink VLC-based MBSNs channel model were experimentally investigated. In [72], an active IR and passive VLC transmission was considered where a Thin-film Corner Cube Retroreflector (TCCR) was employed as a rechargeable battery to modulate and reflect the measurements from the sensors on the body. In [73] and [74], multiple sensors were used and the data was sent as a single combined signal by a VLC transmitter to a receiver. In [75], the Optical Camera Communication (OCC) was utilized in a MBSNs system.

B. MOBILE CHANNEL MODELS

In previous subsection, we overviewed the existing static VLC-based MBSNs channel models. In this subsection, we overview the existing dynamic VLC-based MBSNs channel models where both unidirectional [60]–[62] and bidirectional [63]–[65] channel models are considered.

In [60], the stochastic MCRT method was adopted for CIR modeling with $k = 1$, 3, and 7 reflections inside an empty room with dimensions of 5 m × 5 m × 3 m where four VLC transmitters are placed on the ceiling. Two different mobility scenarios were considered while the patient who wears the receiver walks around the room. In the first scenario, the axes of the receiver location were modelled with a uniform distribution on 2D plane. In the second scenario, the random orientation of the receiver induced by the patient's body movements were modelled according to a uniform distribution. The results revealed that when the elevation and azimuth angles are equal to $\pi/3$, the impact of the NLoS rays on CIR are more pronounced than that of the LoS rays. Therefore, to obtain a more accurate delay spread and ISI information, the CIR with $k = 7$ is needed. On the other hand, when the orientation angle are equal to 0, or perpendicular, the impact of the LoS rays on CIR are more pronounced than that of the reflected rays, i.e., the higher order of reflections does not contribute much in the CIR. The results in [60] also revealed that the effect of receiver orientation does not imply significantly on the channel model performance for the data rates up to 30 Mbps.

In [61], the stochastic MCRT method with $k = 3$ was adopted for the same environment of [60] where double mobility model for the receiver location and orientation was considered. As for the human body modeling, two different models were investigated, i.e., 2D generic body model with dimensions 1.72 m × 0.45 m and highly detailed 3D mesh body model where a thickness of 0.25 m with 1796 facet was integrated into the model. The surface reflection of 2D and 3D bodies were also modelled as purely Lambertian Bidirectional Reflectance Distribution Function (BRDF) with a fixed reflectance value ρ. The optical channel DC gain was obtained for scenarios with (i) absence of the body, (ii) presence of the 2D body with $\rho = 0.7$, (iii) presence of the 3D body with $\rho = 0.7$, (iv) presence of the 2D body with $\rho = 0.1$, and (v) presence of the 3D body with $\rho = 0.1$. The results reveal that a simplistic 2D body model is sufficient for channel modeling if the body reflection is high. Besides, it was observed that the reflectivity is more important than the level of details while modeling a human body.

In [62], the impacts of the physical and geometrical parameters on channel modeling were investigated. An empty room with dimensions of 5 m × 5 m × 3 m was considered where

TABLE 2. Comparison table of studies on downlink VLC-based MBSNs channel models.

	Method	Modeling of Reflectance	Number of Reflections	Other Assumptions	Configuration under Consideration
[59]	Experiment	N/A (LoS)	No reflection	-Empty room -Commercial white LED	The static LoS downlink VLC channel with a diffused transmitter was experimentally established.
[60]	Monte Carlo ray tracing algorithm	Fixed reflectance	Seventh order	-Purely Lambertian -Empty room -Ideal Lambertian source -MISO VLC scheme	The static channel impulse response for an empty room with dimensions of 5 m $\times$ 5 m $\times$ 3 m were modelled. The first, third and seventh order reflections were also considered and the receiver was located at (4.9 m, 4.9 m, 0.8 m) for both $k = 1$ and 7 reflections.
[61]	Monte Carlo ray tracing algorithm	Fixed reflectance	Third order	-Purely Lambertian -Empty room -2D and 3D human body model -Ideal Lambertian source -MISO VLC scheme	The optical channel DC gain was obtained for an empty room with dimensions of 5 m $\times$ 5 m $\times$ 3 m.
[62]	Monte Carlo ray tracing algorithm	Fixed reflectance	Third order	-Diffuse, and mixed reflections -Room with furniture -2D and 3D human body model -Ideal Lambertian source -MISO VLC scheme	An empty room with dimensions of 5 m $\times$ 5 m $\times$ 3 m and different surface materials for the ceiling, walls, and floor were considered. Six configurations were investigated, i.e., (1,2) empty regular bedroom and hospital bedroom, (3,4) regular bedroom and hospital room with 2D body model and furniture, and (5,6) regular bedroom and hospital room with 3D body model and furniture. Various body and receiver orientations were also considered in these configurations.
[63]	Monte Carlo ray tracing algorithm	Fixed reflectance	Third order	-Purely Lambertian -Empty room -2D human body model -Ideal Lambertian source -SIMO IR scheme	The diffuse configuration inside an empty room with dimensions of 6.7 m $\times$ 6.6 m $\times$ 3 m was modelled. The receiver orientations of $\phi = 10^\circ, 20^\circ, 30^\circ, 45^\circ, 60^\circ, 75^\circ$, and 90° were considered in the presence of 2D human body.
[64]	Monte Carlo ray tracing algorithm	Fixed reflectance	Third order	-Purely Lambertian -Empty room -2D human body model -Ideal Lambertian source -SIMO IR scheme -MISO VLC scheme	An empty room with dimensions of 5 m $\times$ 5 m $\times$ 3 m was considered where the effect of various transmitter and receiver orientations in the presence of human body were investigated.
[65]	Monte Carlo ray tracing algorithm	Fixed reflectance	Third order	-Purely Lambertian -Empty room -3D human body model -Ideal Lambertian source -SIMO IR scheme	An empty room with dimensions of 6.7 m $\times$ 6.6 m $\times$ 2.8 m was considered where the impact of various transmitter heights, i.e., $h = 0.2, 0.5, 0.9, 1.2, 1.5$, and 1.7 m, and various reflectivity values, i.e., $\rho = 0.1, 0.5$, and 0.9, in the absence and presence of human body were investigated.

the transmitter oriented towards the floor was fixed on the ceiling and modelled with a Lambertian directivity $m = 1$. The location of a mobile receiver oriented towards the ceiling was also statistically modelled in 2D plane. The coating materials were modelled by purely diffusive (Lambertian), or mixed (Blinn-Phong) models. Six configurations were investigated in [62], i.e., (1, 2) empty regular bedroom and hospital bedroom, (3, 4) regular bedroom and hospital room with 2D body model and furniture, and (5, 6) regular bedroom and hospital room with 3D body model and furniture. The results indicate that the impact of detail-levels supersedes compare to impact of furniture and human body presence in the regular bedroom. On the contrary, the impact of furniture and body presence supersedes compare to impact of detail-levels in the hospital bedroom. It was also observed that the impact of detail-levels increases with an increase in data-rate.

In [63]–[65], a full-duplex bidirectional (i.e., downlink VLC and uplink IR channels) dynamic OWC-based MBSNs channel was presented where the MCRT simulations with $k = 3$ are made for modeling diffuse IR and VLC channels. As for downlink channel, an LED panel of dimensions 0.6 $\times$ 0.6 m was fixed on the ceiling center as an ideal Lambertian source with $m = 1$. A VLC receiver with a perpendicular orientation was also integrated into a tablet which is held in front of the moving patient at fixed height of 1.2 m. The patient location was statistically modelled among 10^4 points on 2D plane. As for uplink channel, an IR transmitter with perpendicular orientation was placed on the shoulder of the moving patient at fixed height of 1.2 m. Four identical IR receivers were also fixed at the corners of LED panel. The results in [63] and [64] revealed that the channel reliability of uplink IR channel with optimal orientation is superior to that of the downlink VLC channel with the body presence. Besides, the precise modeling of human body reflectivity is indispensable for the indoor scenarios with random receiver orientation.

IV. SITE-SPECIFIC MBSNs CHANNEL MODELING

In previous sections, we reviewed the existing OWC-based MBSNs channel models. In this section, we introduce the site-specific MBSNs channel modeling method using

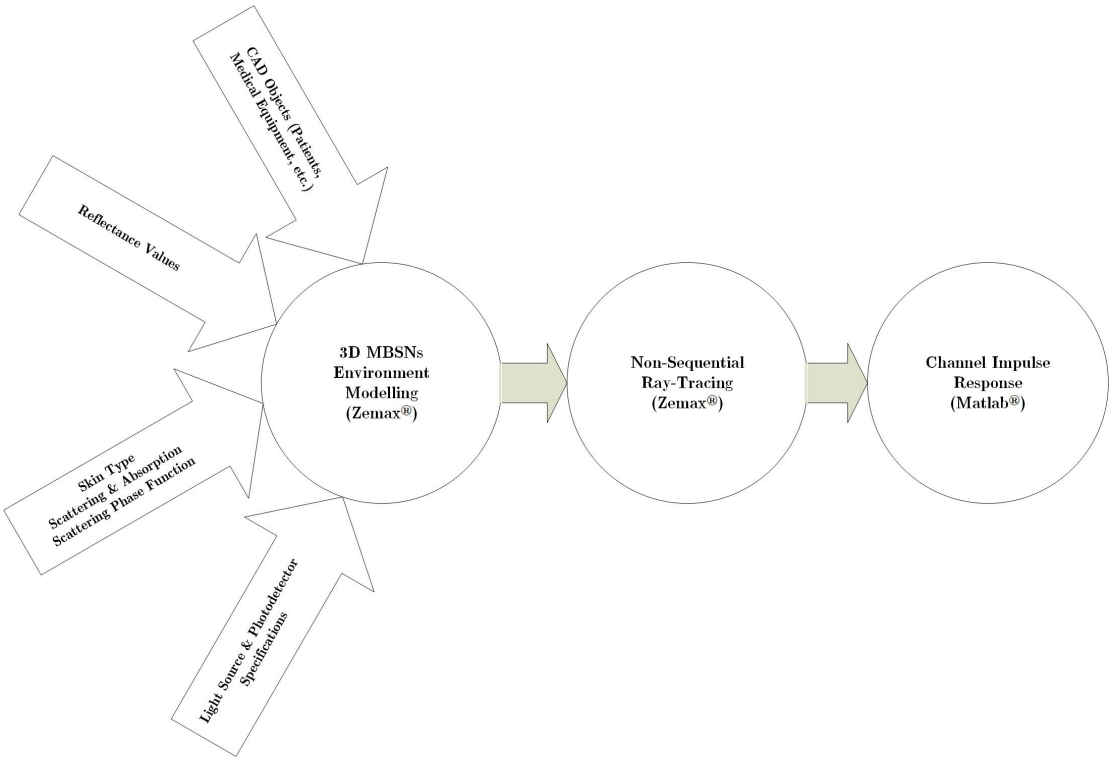

FIGURE 2. Main steps of site-specific channel modeling for VLC-based MBSNs.

advanced non-sequential ray tracing tool of Zemax® [47]. In this software, there are two modes of ray tracing. In sequential ray tracing, rays are traced through a sequence of surfaces, hitting each surface only once, while traveling from the transmitter to the receiver. This property makes sequential mode ideal for imaging systems. On the other hand, non-sequential ray tracing allows rays to propagate through environment in any order and allows rays to be scattered and reflected back to an object that they have already encountered. This property makes non-sequential mode ideal for impulse response modeling which is adopted in our study.

Our approach obtains CIRs for various indoor environments with diverse room-dimensions and assumes integration of realistic light sources in the simulation environment. Furthermore, many reflections (more than 10) can be easily handled for better accuracy including specular and mixed specular-diffuse reflections. Major steps of the proposed MBSNs channel modeling approach are illustrated in Fig. 2. In the first step, we create a 3D simulation environment where we can specify the geometry of the indoor environment, the objects within, the reflection characteristics of the surface materials, the absorption, scattering and scattering phase function of human skin, and the specifications of the light sources and detectors. In the second step, we use non-sequential ray tracing to calculate the detected power and path lengths from source to detector for each ray. In the third step, we import this data to Matlab® and obtain the CIRs for the considered scenario.

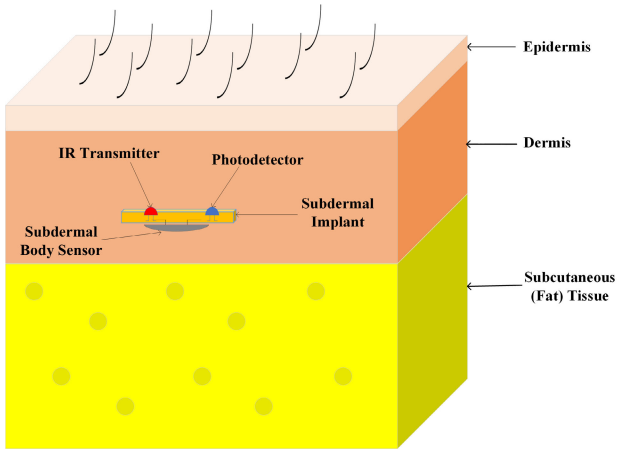

FIGURE 3. Subdermal sensor placement in conventional three-layered skin model.

A. OPTICAL CHARACTERIZATION OF HUMAN SKIN

The main optical characteristics of tissues in VL spectrum are the wavelength-dependent refractive index $n(\lambda)$, absorption coefficient $\mu_a(\lambda)$, scattering coefficient $\mu_s(\lambda)$, anisotropy factor $g(\lambda)$ (i.e., the average cosine of scattering angle in all scattering directions), and scattering phase function [76]. Water makes up the large part of the most tissues and it has the minimum refractive index among all tissue components. Moreover, water is measured as the dominant absorption molecule in IR spectrum whereas hemoglobin and melanin

TABLE 3. MBSNs applications.

Clinical applications	Sensor location	Sensor types
Glucose home monitoring	Subcutaneous	Glucose
	Eye	Glucose
	Arm	Multi-variable
Cardiopulmonary and vascular monitoring	Wrist	Ultrasound
		Multi-variable
		Photoplethysmograph (PPG) Electrocardiograph (ECG)
	Finger (ring sensor)	Optical (heart rate)
		Radio-frequency identification
	Arm or thigh	Microwave reflectometric cardiopulmonary
	Compatible with various equipment	Optical sensor
		ECG electrodes
	Phone adapter	Single-channel ECG
	Seat belt of a car	Wired strain gauge
Neurological function monitoring	Clothes	Inertial sensors Accelerometers
	Visual feedback-glasses	Inertia
	Auditory feedback-headphones	
	Wrist or ankle	Accelerometer Motion
Physical therapy and rehabilitation	Ankle	Pedometers Accelerometer

TABLE 4. Various multilayered skin models.

Three-layered model [81]	Seven-layered model [82]	Nine-layered model [81]
Epidermis (Blood-free layer)	Stratum corneum	Stratum corneum
	Living epidermis	Stratum granulosum, Stratum spinosum
		Stratum basale
Dermis (Vascularized layer)	Papillary dermis	Papillary dermis
		Subpapillary dermis
	Upper blood net dermis	Upper blood net dermis
	Reticular dermis	Reticular dermis
	Deep blood net dermis	Deep blood net dermis
Subcutaneous tissue (Fat layer)	Subcutaneous tissue	Subcutaneous tissue

are the dominant ones in VL range. The most appropriate frequency range to mitigate the absorption effects is between the red to near-IR spectrum, i.e., 600-1300 nm and called as the diagnostic and therapeutic window. Experiments have been also conducted on ex-vivo human skin using Monte-Carlo inversion technique in [77]. Integrating sphere has been used for the reflectance and transmittance measurements by sending collimated beam in wavelengths between 620 to 1000 nm. The absorption and scattering coefficients depending on these wavelengths are obtained for dermis, fat, and muscle layers of the skin. It is observed that the absorption coefficient decreases while the wavelength is increasing until 825 nm. Then, it starts to rise until 1000 nm. On the other hand, scattering coefficient shows a gradual reduction while the

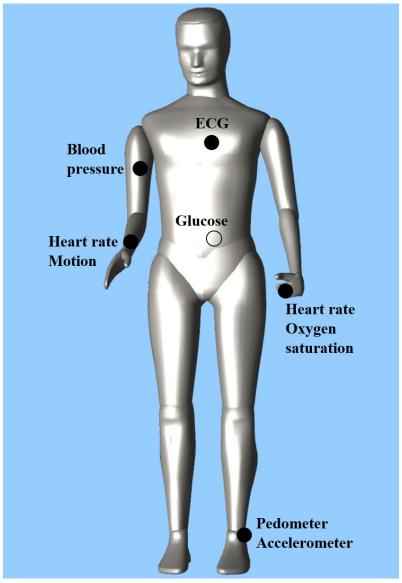

FIGURE 4. Typical MBSN node locations.

wavelength is increasing. The experiment results in [77] also show that the skin tissue comprising epidermis, dermis, and fat layers with 11.5 mm thickness allows significant power transmission.

For most biological tissues, the anisotropy factor is approximately 0.9 which corresponds to anisotropic forward scattering. There are also some other key factors determining the quality of Transdermal Communication (TC) channel between the implanted transceiver and on-body transceiver (see Fig. 3) such as the skin tissue thickness, the size of the integration area of the optics, optics system efficiency factor, the amount of misalignment, and the transmitter power [78].

To model scattering phase function, One-Term Henyey-Greenstein (OTHG) scattering phase function $P(\vartheta)$ fits well when approximating the human skin [79]. It is described by only a single parameter, i.e., the anisotropy factor, as [80]

$$P(\vartheta) = \frac{1}{4\pi} \frac{1 - g^2}{(1 + g^2 - 2g\cos\vartheta)^{3/2}} \tag{3}$$

where ϑ is the longitudinal scattering angle.

Medical body sensors are also categorized based on their locations (see Fig. 4), usage areas, and clinical applications [83] (see Table 3). For example, subcutaneous sensors measuring the glucose level in the body are used in glucose home monitoring applications.

There are also conventional skin models in the literature, i.e., three-layered skin model [81] which comprises epidermis, dermis, and subcutaneous tissues; seven-layered [82] and nine-layered [81] skin models. The multilayered skin models are detailed in Table 4. The absorption and scattering coefficients of three-layered model are presented in Fig. 5 [84].

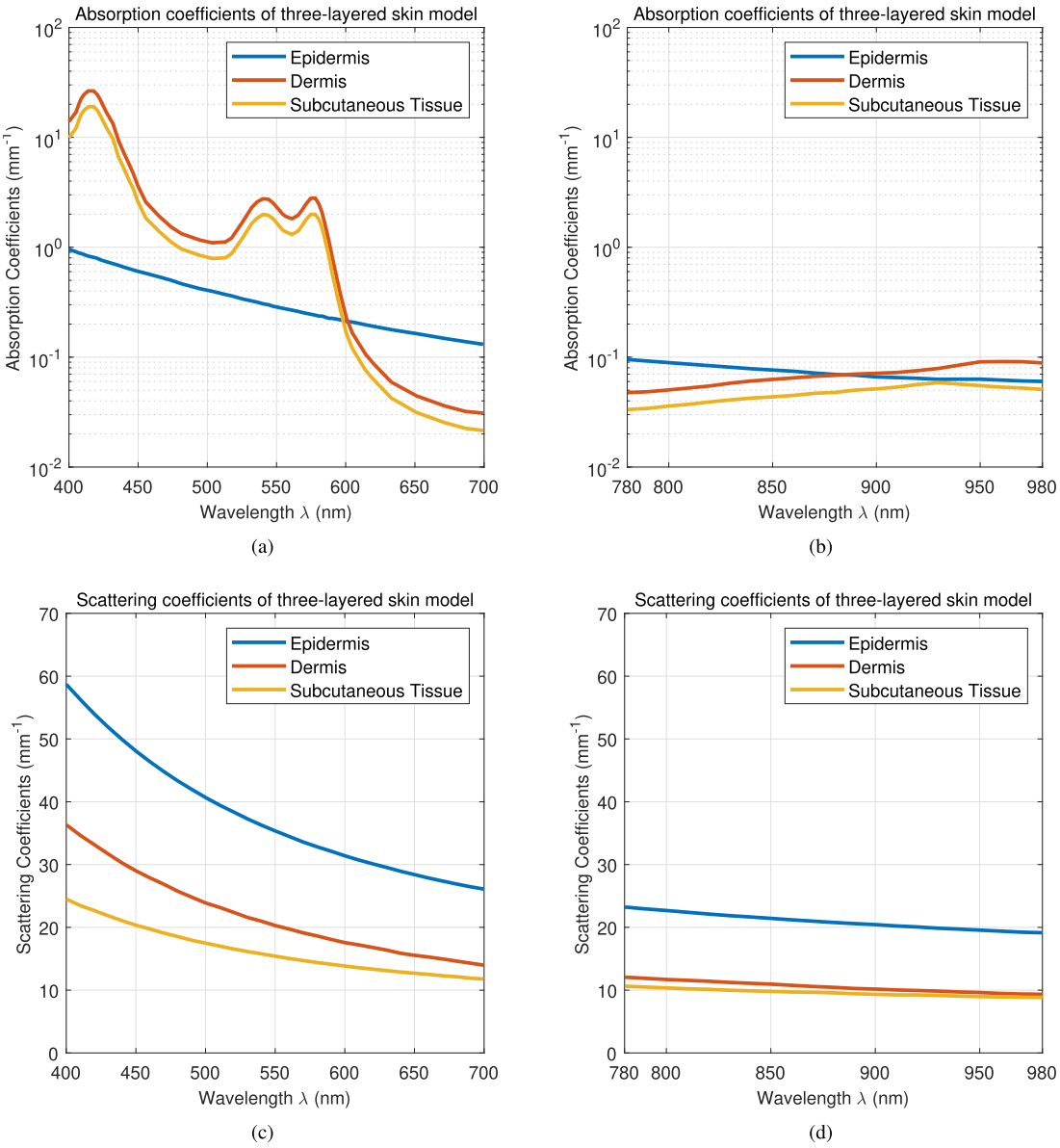

FIGURE 5. (a-b) Absorption and (c-d) scattering coefficients of human skin in three-layered skin model for VL band (400-700 nm) and IR band (780-980 nm) [84].

Based on the key factors described above, the received power in TC channel is calculated as

$$P_r = \int_A P\, J_{Rx\lambda}\, \eta_\lambda\, dA \tag{4}$$

where P is optical transmitted power, $J_{Rx\lambda}$ is spatial optical power distribution on the skin at wavelength λ, η_λ is the efficiency factor, and A is the tissue area.

B. METHODOLOGY

Based on Table 1 and 2, it is inferred that MCRT is widely used in the literature as a more flexible tool for channel modeling. This statistical method can determine the channel characteristics by generating numerous photons and then simulating the interactions of each photon with the medium. The MCRT allows importing the key parameters of TC channel such as refractive index, absorption coefficient, scattering coefficient, and scattering phase function. The refractive index determines the photon reflection and refraction at Fresnel boundaries between the tissue layers which defines the speed of light within the tissue and the manner in which photons penetrate tissue. Although the refractive index is wavelength dependant, according to the measured data reported in [77] and [85], the refractive indices of epidermis, dermis, and fat layers are set to $n = 1.4$ (see Table 5). The absorption and scattering coefficients define the probability of a photon to be absorbed and scattered per unit length, respectively. Based on Fig. 5, the average values of $\mu_a(\lambda)$ and

TABLE 5. Simulation parameters for the adopted three-layered skin model in the proposed site-specific channel modeling.

Layers	Thickness (μm) [82]	$\bar{\mu}_a$ (λ) (mm^{-1}) [84]		$\bar{\mu}_s$ (λ) (mm^{-1}) [84]		Mean free path		Photon weight updating		n [85]	g [77]
		VLC	IR	VLC	IR	VLC	IR	VLC	IR		
Epidermis	100 – 120	0.3701	0.0730	37.7195	20.9302	0.0263	0.0476	0.9903	0.9965	1.4	0.9
Dermis	1710 – 2200	3.6640	0.0690	21.9560	10.5482	0.0390	0.0942	0.8570	0.9935		
Subcutaneous tissue	6000 – 6500	2.6085	0.0469	16.3183	9.5971	0.0528	0.1037	0.8622	0.9951		

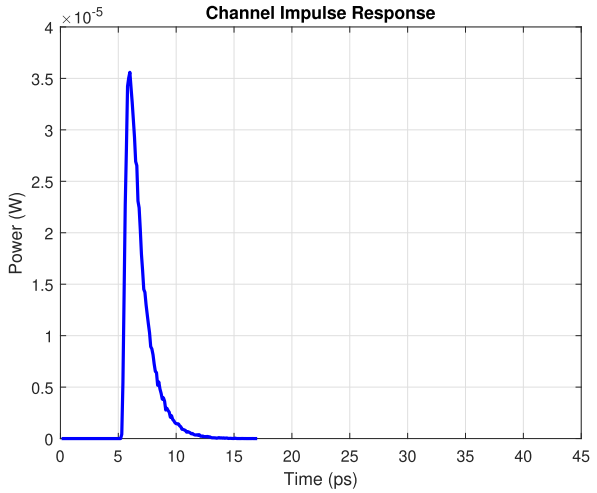

(a)

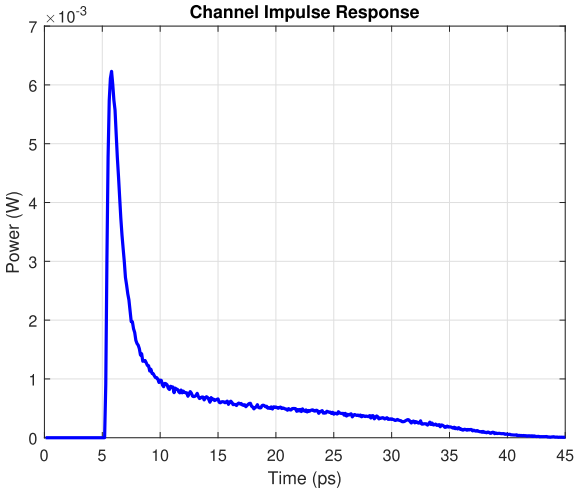

(b)

FIGURE 6. Skin channel models for (a) downlink VLC from epidermis to dermis, and (b) uplink IR from dermis to epidermis.

μ_s (λ) over 400 – 700 nm (i.e., the spectrum of VL source) and 780 – 980 nm (i.e., the spectrum of IR source), are computed for three-layered skin model (see Table 5).

The scattering phase function $P(\vartheta)$ defines the PDF for scattering in a direction at an angle ϑ relative to the direction of the traveling photon. In human skin modeling, OTHG scattering phase function provides the most realistic approximation [86]. The OTHG formula is modelled with three parameters which are mean free path, photon weight updating, and anisotropy factor [86]. The mean free path which defines the average distance covered by propagating photons before a scattering event occurs is given by

$$\text{Mean Free Path} = \frac{1}{\mu_a + \mu_s}. \tag{5}$$

The photon weight updating which defines the change in weight of transmitting photon after occurrence of absorption and scattering events during its travel is given by

$$\text{Photon Weight Updating} = \frac{\mu_s}{\mu_a + \mu_s}. \tag{6}$$

The anisotropy factor defines the mean cosine of scattering angle ϑ. This parameter changes between -1 and 1 such that minus unity, zero and unity indicates total backscattering, isotropic (Rayleigh) scattering, and total forward-scattering (Mie), respectively. In biological tissues, Rayleigh scattering contributes due to small-scale structures whereas Mie scattering contributes due to collagen fibres in skin tissue [81]. The mean free path, photon weight updating, and anisotropy factor for the adopted three-layered skin model in the proposed downlink VLC and uplink IR skin channel models are summarized in Table 5. It should be noted that there is a trade-off between skin thickness and power efficiency. Choosing an implant location with a very thin dermal covering provides a very significant power advantage [78]. In that respect, the subdermal sensor in conventional three-layered skin model is placed within dermis layer due to smaller thickness of dermis and epidermis layers. Therefore, only the refractive index of these two layers are of importance in skin tissue channel modelling.

Based on the approach summarized above, the skin channel model can be realized by considering the uplink and downlink channels separately. The thickness of epidermis and dermis layers are selected as 100 μm and 2000 μm, respectively. The implant is placed in the middle of dermis layer and hence the distance between transmitter and receiver is 1100 μm. We consider the IR and VL transmitters with the same half viewing angle of 60 degrees and the FOV and the area of the detector for both channels are 90° and 1 cm^2, respectively. A total unit (normalized) power is assumed for both IR and VL transmitters. The perfect alignment configuration is considered for both uplink and downlink channels. Downlink VLC and uplink IR skin channel models obtained through the proposed site-specific MBSNs channel modeling approach are presented in Figs. 6a and 6b, respectively. It is observed that the maximum received power is 35.69 μW at 6 ps for the downlink VLC channel (i.e., from epidermis to dermis) whereas it peaks at 6.23 mW at 5.8 ps for the uplink IR channel (i.e., from dermis to epidermis). Besides, the delay spread values of the downlink VLC channel and uplink IR

channel are around 10 ps and 40 ps, respectively. These discrepancies are due to this fact that the optical properties of skin tissue layers are wavelength-dependent, and the emitted rays from VL transmitter in downlink VLC channel traverses from epidermis to dermis layer while the emitted rays from IR transmitter in uplink IR channel traverses from dermis to epidermis.

C. CHANNEL MODELING IN REAL-LIFE BASED HOSPITAL SCENARIOS

In this section, based on the proposed approach summarized in Section IV, we model the channels of four MBSNs reference scenarios, i.e., Intensive Care Unit (ICU) ward, clinic, semi-private patient room, and family-centered patient room (see Fig. 7). These scenarios are constructed as per requirements in [87][1] and [88]. The specifications of the reference scenarios are detailed in Table 6. The coating materials of objects in scenarios under consideration are summarized in Table 7. Next, we describe each of these scenarios accompanied with corresponding CIRs.

For predefined number of rays, the advanced ray tracing calculates the path length and detected power of each ray launched from transmitter to receiver. These are further processed in Matlab® to obtain the CIR as

$$h_{\mathrm{VLC}}(t) = \sum_{i=1}^{N_r} P_i\, \delta(t - \tau_i), \tag{7}$$

where P_i is the received power of the i^{th} ray, τ_i is the propagation time of the i^{th} ray, $\delta(t)$ is the Dirac delta function and N_r is the received number of rays.

A VLC-based MBSNs channel is characterized by the channel DC gain which is the collected portion of the launched rays, and it is expressed as

$$H_0 = \int_0^{+\infty} h_{\mathrm{VLC}}(t)dt. \tag{8}$$

Another essential channel characteristic is the RMS delay spread, which is a metric presenting the temporal dispersion of the multipath transmission, and it is defined as

$$\tau_{RMS} = \sqrt{\frac{\int_0^{+\infty} (t-\tau_0)^2\, h_{\mathrm{VLC}}(t)dt}{\int_0^{+\infty} h_{\mathrm{VLC}}(t)dt}} \tag{9}$$

where τ_0 is the mean delay spread.

$$\tau_0 = \int_0^{+\infty} t\; h_{\mathrm{VLC}}(t)dt \Big/ \int_0^{+\infty} h_{\mathrm{VLC}}(t)dt \tag{10}$$

[1]The Facility Guidelines Institute (FGI)'s guidelines are US-based guidelines that can be globally applied for design and construction of healthcare facilities. The Health Guidelines Revision Committee (HGRC) is the multidisciplinary group responsible for revising the guidelines documents and it is composed of approximately 100 clinicians, administrators, architects, engineers, and representatives from authorities having jurisdiction and they are subject matter experts in health care design and practice.

TABLE 6. Specifications of scenarios under consideration.

Features	ICU ward	Clinic	Semi-private patient room	Family-centered patient room
Number of beds	4	1	2	1
Number of bodies	5	3	4	3
Number of sources	15	5	8	8
Number of PDs	16	6	8	4
Dimensions (L×W×H) (m)	11.5×6.5×3	5×4×3	8.8×5×3	7×5×3
Clear floor area per bed (m^2) [87], [88]	13.69	14	14.13	23.66
Side clearance on non-transfer side of bed (m) [87]	≈ 1	≈ 1	≈ 1	≈ 1
Side clearance on transfer side of bed (m) [87]	1.5	$\gg 1.22$	2	$\gg 1.22$
Clearance at the foot of each bed (m) [87]	2.3	1.7	2.3	2.3

TABLE 7. Coating materials for the scenarios under consideration.

Scenario 1 ICU ward	walls: plaster, ceiling: plaster, floor: pinewood, hospital bed: aluminium, ICU desk: pinewood, chair: black gloss paint
Scenario 2 Clinic	walls: plaster, ceiling: plaster, floor: pinewood, hospital bed: aluminium, medical ultrasound machine: aluminium, desk: pinewood, chair: black gloss paint, laptop: black gloss paint
Scenario 3 Semi-private patient room	walls: plaster, ceiling: plaster, floor: pinewood, WC door: pinewood, curtain: cotton, hospital bed: aluminium, chair: black gloss paint, drawer: pinewood, wardrobe: pinewood
Scenario 4 Family-centered patient room	walls: plaster, ceiling: plaster, floor: pinewood, WC door: pinewood, hospital bed: aluminium, chair: black gloss paint, drawer: pinewood, wardrobe: pinewood, sofa cover: cotton, side tables: pinewood, coffee table: pinewood

1) ICU WARD

In this scenario, an ICU ward which consists of four patients laying on their beds, and a continuously working medical staff standing in front of her desk and chair, is considered (Fig. 7a). The dimensions of ICU ward is 11.5 m × 6.5 m × 3 m where 15 luminaires are uniformly located on the ceiling. The luminaires in MBSNs reference scenarios under consideration are commercially available from Cree® 14-40LHE with a half viewing angle of 55 degrees and 125 lumens per watt efficacy. As illustrated in Fig. 8a, the illuminance uniformity (i.e., as the ratio of the minimum illuminance to the average one), minimum, maximum and average values of illumination are calculated as 0.89, 72.93 lx, 89.71 lx, and 82.30 lx, respectively which meet the illumination requirements of ICU ward [89], [90]. Sixteen different locations are considered for PDs (D1, . . . , D16).[2] A PD is located on the

[2]It is possible to improve signal-to-noise ratio (SNR) by narrowing the receiver FOV through the use of a proper lens. However, a narrow FOV might be problematic for mobile conditions. Therefore, we prefer a large FOV (i.e., 90 degrees) in this study to maximize reception angle.

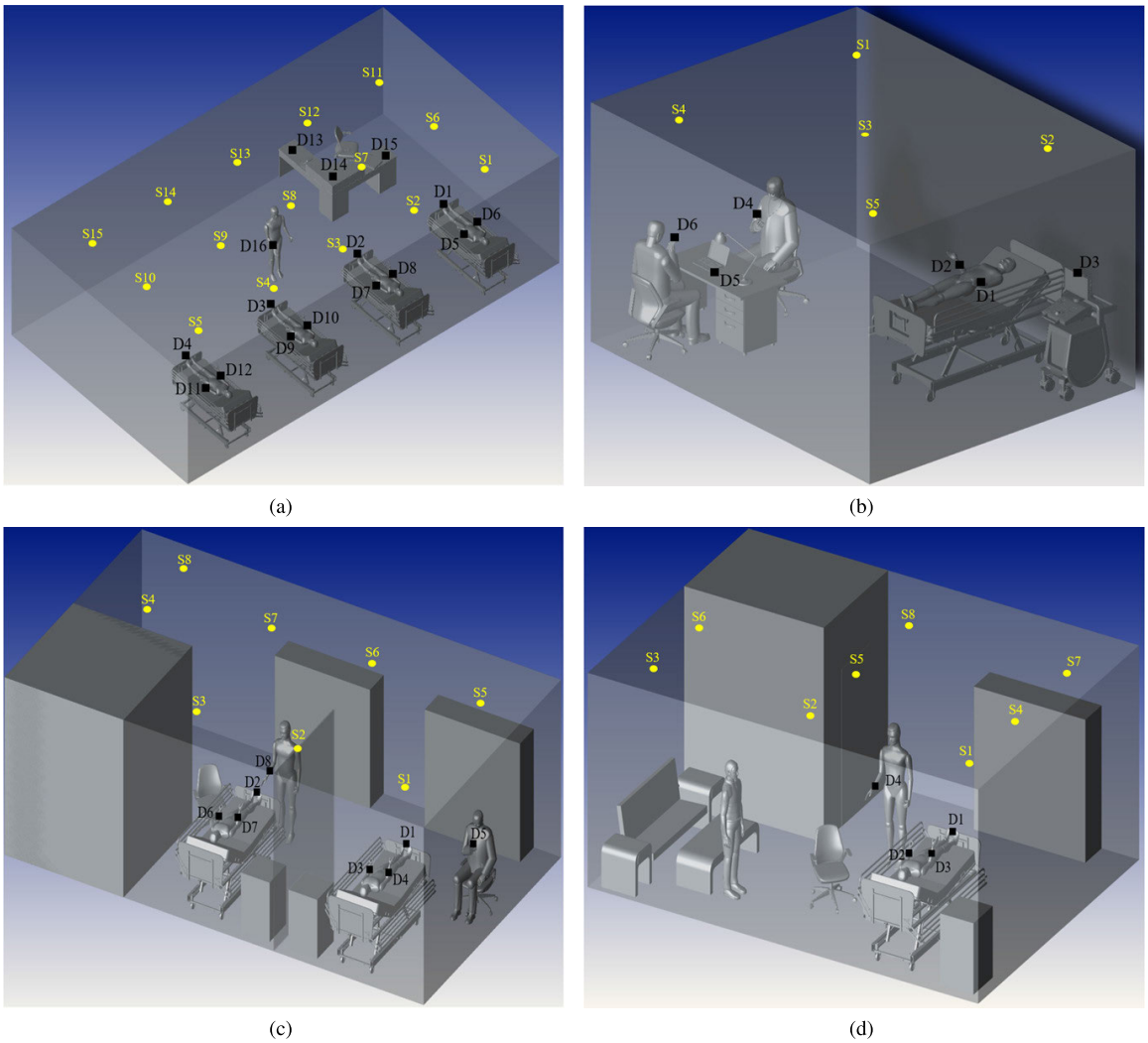

FIGURE 7. Scenarios under consideration: (a) ICU ward, (b) clinic, (c) semi-private patient room, and (d) family-centered patient room.

top side of the foot plate of each patient bed, a pair of PDs is placed on right and left inner arms of each laying patient, a PD is positioned on the wrist of the medical staff, and three PDs are placed on the corners of L-shape desk in the environment.

The sample CIRs for the scenario under consideration are shown in Figs. 9a–9d. It is observed from Fig. 9a that the LoS rays are dominant. This is due to the fact that a nurse wearing a smartwatch upon which a detector D16 is placed, stands just under the VLC source. It is also observed from Fig. 9b that the diffused rays are dominant since the detector D11 on MBSN node worn by the patient is far from the VLC source and many objects are placed between them.

2) CLINIC

In this scenario, a clinic which consists of single patient laying on the bed next to the medical ultrasound device, and a medical doctor and patient's companion sitting opposite while both holding their cell phones is considered (Fig. 7b). The dimensions of the clinic is 5 m $\times$ 4 m $\times$ 3 m where 5 luminaires are uniformly located on the ceiling. As illustrated in Fig. 8b, the illuminance uniformity, minimum, maximum and average values of illumination are calculated as 0.78, 407.70 lx, 611.80 lx, and 521.38 lx, respectively which meet the illumination requirements of a clinic [89], [90]. Six different locations are also considered for PDs (D1, . . . , D6). A PD is located on the top side of the medical ultrasound device screen, a pair of PDs is placed on right and left inner arms of the laying patient, a PD is positioned on the top of each cell phone of doctor and patient's companion, and the last PD is located on top of a USB inserted to laptop computer.

The sample CIRs for this scenario are shown in Figs. 9e–9h. It is observed from Fig. 9e that the LoS rays are dominant since the detector D1 on MBSN node worn by the patient is located in close proximity to the VLC source with negligible path-obstructions. It is further observed from

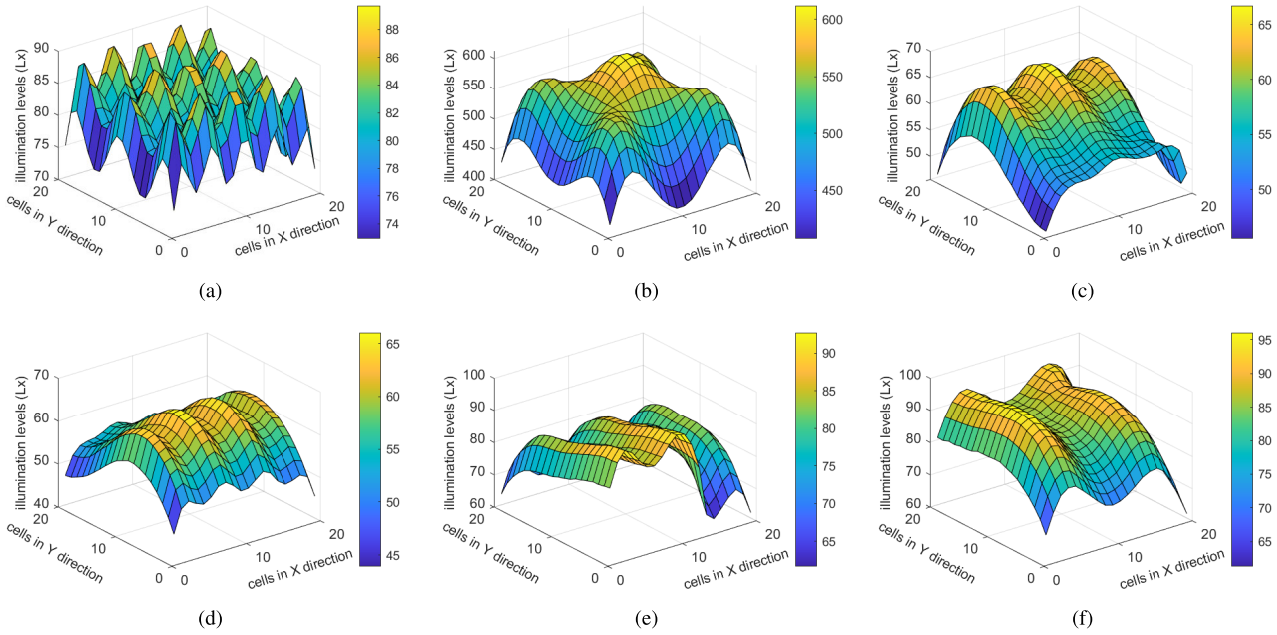

FIGURE 8. Illumination levels for (a) ICU ward, (b) clinic, (c, d) semi-private patient room, and (e, f) family-centered patient room.

Fig. 9f that the diffused rays are significant since the patient companion holding the cell phone upon which the detector D4 is placed, partially shadows the rays coming from the near VLC source. The diffused rays are also observed in the CIR of Fig. 9g which is due to the fact that the detector D5 on USB flash drive which is connected to the laptop is partially shadowed by the desk lamp.

3) SEMI-PRIVATE PATIENT ROOM

In this scenario, a semi-private patient room consisting of two patients lying on their beds, a standing medical staff, and a patient's companion sitting at the bottom side of the corresponding patient's bed is considered. Moreover, a curtain is placed between the drawers next to the patient beds, and wardrobes for each patient are located against the beds (Fig. 7c). The dimensions of semi-private patient room is 8.8 m $\times$ 5 m $\times$ 3 m that includes a toilet with dimensions 2.5 m $\times$ 2.5 m $\times$ 3 m. There are 8 luminaires uniformly located on the ceiling. Due to existence of a toilet room, the room is divided into two sections, with the first section containing the patient's beds and the second one containing the wardrobes. As illustrated in Fig. 8c, for the first section, the illuminance uniformity, minimum, maximum and average values of illumination are respectively calculated as 0.78, 45.53 lx, 66.69 lx, and 58.21 lx while they are respectively calculated as 0.76, 43.92 lx, 66.04 lx, and 57.97 lx for the second section of the room (Fig. 8d). It is observed that the illumination requirements for whole room can be satisfied as per requirements in [89] and [90]. Eight different locations are also considered for PDs (D1, . . . , D8). A PD is located on the top side of the foot plate of each patient bed, a pair of PDs is placed on right and left inner arms of each laying patient, a PD is positioned on the wrist of the medical staff, and the last PD is placed on top of the cell phone of patient's companion.

The sample CIRs for this scenario are shown in Figs. 9i–9l. It is observed from Fig. 9i that the LoS rays are dominant since the detector D7 on MBSN node worn by the patient is located in close proximity to the VLC source located at top of the limited-height thin curtain. It is also observed from Fig. 9j that diffused rays are dominant since the patient companion holding the cell phone upon which the detector D5 is placed, partially shadows the rays coming from the far VLC source. Moreover, only diffused rays are observed in the CIR of Fig. 9l which is due to the fact that the LoS link between the detector D3 on MBSN node worn by the patient and the VLC source placed next to toilet is blocked by separating curtain.

4) FAMILY-CENTERED PATIENT ROOM

In the last scenario, a family-centered patient room which consists of a single patient laying on the bed, a standing medical staff, and a patient's companion standing in front of the sofa bed and coffee table set is considered. Moreover, a drawer placed next to the patient bed, and a wardrobe is located against the beds (Fig. 7d). The dimension of semi-private patient room is 7 m $\times$ 5 m $\times$ 3 m including a toilet whose dimension is 2.5 m $\times$ 2 m $\times$ 3 m. There are 8 luminaires uniformly located on the ceiling. Due to existence of a toilet room, we divide the room into two sections, i.e., the first section contains the patient's bed and the second one contains the wardrobe. As illustrated in Fig. 8e, for the first section of the room, the illuminance uniformity,

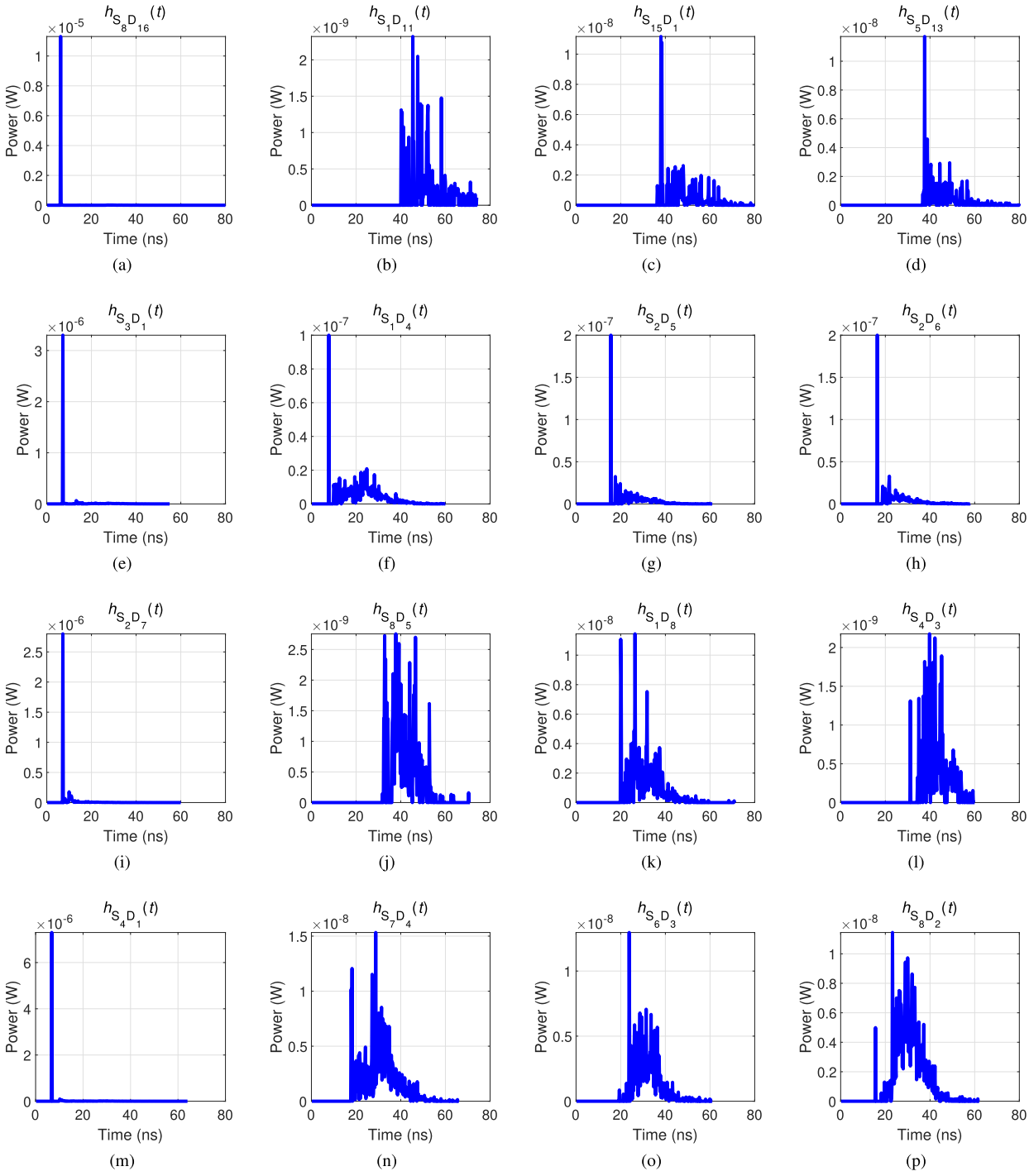

FIGURE 9. Sample CIRs for (a-d) ICU ward, (e-h) clinic, (i-l) semi-private patient room, and (m-p) family-centered patient room.

minimum, maximum and average values of illumination are respectively calculated as 0.77, 61.66 lx, 92.74 lx, and 80.34 lx while they are respectively calculated as 0.71, 61.34 lx, 96.04 lx, and 85.83 lx for the second section of the room (Fig. 8f). Four different locations are also considered for PDs (D1, . . . , D4). A PD is located on the top side of the foot plate of each patient bed, a pair of PDs is placed on right and left inner arms of each laying patient, and the last PD is positioned on the wrist of the medical staff.

The sample CIRs for this scenario are shown in Figs. 9m–9p. It is observed from Fig. 9m that the LoS rays are dominant since the bed footboard on which detector D1 is placed stands just under the VLC source. It is also observed from Fig. 9n that the NLoS rays are dominant since a nurse

TABLE 8. Channel characteristics.

Scenario	Sample CIR	H_0	τ_{RMS} (ns)
ICU Ward	$h_{S_8D_{16}}(t)$	2.38×10^{-6}	5.70
	$h_{S_1D_{11}}(t)$	7.64×10^{-9}	7.89
	$h_{S_{15}D_1}(t)$	2.02×10^{-8}	8.78
	$h_{S_5D_{13}}(t)$	1.64×10^{-8}	7.98
Clinic	$h_{S_3D_1}(t)$	8.48×10^{-7}	8.04
	$h_{S_1D_4}(t)$	1.95×10^{-7}	9.18
	$h_{S_2D_5}(t)$	1.60×10^{-7}	8.00
	$h_{S_2D_6}(t)$	1.69×10^{-7}	7.45
Semi-Private Patient Room	$h_{S_2D_7}(t)$	8.83×10^{-7}	5.29
	$h_{S_8D_5}(t)$	1.68×10^{-8}	5.82
	$h_{S_1D_8}(t)$	4.07×10^{-8}	7.26
	$h_{S_4D_3}(t)$	9.60×10^{-9}	5.50
Family-Centered Patient Room	$h_{S_4D_1}(t)$	1.70×10^{-6}	6.13
	$h_{S_7D_4}(t)$	7.73×10^{-8}	7.67
	$h_{S_6D_3}(t)$	5.09×10^{-8}	5.86
	$h_{S_8D_2}(t)$	8.01×10^{-8}	5.89

wearing on her right hand side a smartwatch upon which a detector D4 is placed shadows the VLC source located in the rear left side. It is indeed noteworthy that the frequency selectivity arises mainly due to the multipath reflections (i.e., the NLoS components), however, the deep fade in the frequency response is due to the existence of multiple luminaires due to which multiple LoS components with different delays are received at the photodetector.

The channel characteristics of sample CIRs for reference scenarios under consideration are also summarized in Table 8. It is observed from Table 8 that the channel DC gains depend on the user location and node location on the patient's body. In fact, the mobility of the MBSNs nodes in an environment causes fluctuations in the received power which necessitates the use of link adaptation to combine the LEDs in a most efficient way and selects modulation order. Furthermore, it is observed from Table 8 that the RMS delay spread is in the range 5.29 ns - 9.18 ns. This indicates that for signaling rates lower than 10.89 Msample/sec which can be easily justified for practical needs in MBSNs application, the multipath components are not resolvable and the channel can be modeled as a single-tap (frequency-flat) channel.

In addition to the multipath propagation environment, the effect of LED source should be further taken into account in channel modeling. The frequency response of the LED is assumed as [45]

$$H_{\text{LED}}(f) = \frac{1}{1 + jf/f_{cut-off}}. \tag{11}$$

The effective channel frequency response (taking into account the LED characteristics and the skin channel) can be then expressed as $h_{\text{eff}}(t) = h_{\text{LED}}(t) \otimes h_{\text{Skin}}(t) \otimes h_{\text{VLC}}(t)$, or $H_{\text{eff}}(f) = H_{\text{LED}}(f)\, H_{\text{Skin}}(f)\, H_{\text{VLC}}(f)$, where $H_{\text{Skin}}(f)$ and $H_{\text{VLC}}(f)$ denote the frequency responses of the skin and VLC channels, respectively.

V. FUTURE WORKS

Although we addressed the major issues that researchers have been encountered, there are still many challenges we must work on to obviate. These open issues are summarized briefly as below.

If a patient wearing an MBSN node on the front side, falls on the ground then corresponding MBSN node may not communicate with the other end that should be calling for help, due to the complete blockage. Therefore, diversity techniques could be potentially applied to tackle this vital issue.

Wireless technology requires low power consumption which is especially true for subdermal MBNS nodes. Replacement or charging of the implanted MBSN node is extremely difficult. Thus, energy harvesting, which is the utilization of the ambient energy can be a solution to this critical issue.

Patient body movement induces the mobility of sensor-coupled transceiver in terms of location and orientation. Although obtaining a CIR for each sample point through randomly generated trajectory mitigated the problem of uncertainty, it is still a significant challenge for channel modeling and characterization of MBSNs.

Moreover, the mobility of the MBSNs nodes in an environment causes fluctuations in the received power. An appropriate model for link adaptation which combines LEDs in a most efficient way and selects modulation order, can be proposed to overcome this challenge.

Furthermore, the non-linearity of an LED source, multipath time dispersion, and the mobility of MBSNs node establish a time-varying VLC channel model. To obviate these channel capacity-limiting problems, a pre-distortion technique or a more realistic post-distortion technique can be proposed in the future works of the researchers. This indeed calls for the joint application of reproducing kernel Hilbert space (RKHS) based methods with information theoretic learning (ITL). Regarding these methods, recent works for different applications as VLC, massive MIMO, multiple-access localization [91]–[96] provide rigorous analytical results for the scenario-invariant and system-independent optimality of these approaches in presence of unknown nonlinearities and impairments.

VI. CONCLUSION

In this paper, we presented a comprehensive overview of the VLC-based medical body sensor networks channel modeling which enables researchers to design their systems in best possible QoS. We first analyzed existing IR-based MBSNs channel models from which VLC channel models are derived. Thereafter, we scrutinized existing VLC-based MBSNs channel models according to the mobility of the MBSNs on the patient's body. Our main criticisms among many other simplistic assumptions are the omission of the wavelength-dependency in modeling of the surface reflectance in VLC systems and lack of a proper skin channel model.

Moreover, we presented a novel approach for VLC-based channel modeling and characterization of the skin tissue. It was observed from these channel models that the detected

rays which had experienced less number of events and hence the delays, manifested themselves as a steeper line in CIR. On the other hand, a gradual decrease in received power occurred due to the collection of power losing scattered rays.

Furthermore, we designed four different real-life based hospital scenarios to model and characterize the downlink VLC-based MBSN channels. For this reason, we utilized a site-specific non-sequential MCRT method to obtain CIRs in: i) ICU ward; ii) clinic; iii) semi-private hospital room; and iv) family-centered hospital room. We then presented four sample CIRs for each scenario and their corresponding inferences. The effect of LED emitters were also taken into account to obtain the effective channel frequency response.

We hope that this paper will serve as a valuable resource for understanding the main concerns in VLC-based MBSNs channel modeling and hopefully prompt further research efforts for the design of this promising technology as a powerful complementary technology to its RF counterpart.

REFERENCES

[1] S. Arnon, J. Barry, G. Karagiannidis, R. Schober, and M. Uysal, *Advanced Optical Wireless Communication Systems*, 1st ed. Cambridge, U.K.: Cambridge Univ. Press, 2012.

[2] Z. Ghassemlooy, W. Popoola, and S. Rajbhandari, *Optical Wireless Communications: System and Channel Modelling With MATLAB*, 1st ed. Boca Raton, FL, USA: CRC Press, 2017.

[3] D. Karunatilaka, F. Zafar, V. Kalavally, and R. Parthiban, "LED based indoor visible light communications: State of the art," *IEEE Commun. Surveys Tuts.*, vol. 17, no. 3, pp. 1649–1678, 3rd Quart., 2015.

[4] S. Arnon, *Visible Light Communication*, 1st ed. Cambridge, U.K.: Cambridge Univ. Press, 2015.

[5] S. Dimitrov and H. Haas, *Principles of LED Light Communications: Towards Networked Li-Fi*, 1st ed. Cambridge, U.K.: Cambridge Univ. Press, 2015.

[6] Z. Ghassemlooy, L. N. Alves, S. Zvanovec, and M. A. Khalighi, *Visible Light Communications: Theory Application*, 1st ed. Boca Raton, FL, USA: CRC Press, 2017.

[7] A. Julien-Vergonjanne, S. Sahuguède, and L. Chevalier, "Optical wireless body area networks for healthcare applications," in *Optical Wireless Communications: An Emerging Technology*, M. Uysal, C. Capsoni, Z. Ghassemlooy, A. Boucouvalas, and E. Udvary, Eds. Cham, Switzerland: Springer, 2016, pp. 569–587.

[8] *Medical Electrical Equipment—Part 1-2: General Requirements for Basic Safety and Essential Performance-Collateral Standard: Electromagnetic Disturbances-Requirements and Tests*, document IEC 60601-2, 2014.

[9] T. Cogalan and H. Haas, "Why would 5G need optical wireless communications?" in *Proc. IEEE 28th Annu. Int. Symp. Pers., Indoor, Mobile Radio Commun. (PIMRC)*, Oct. 2017, pp. 1–6.

[10] P. H. Pathak, X. Feng, P. Hu, and P. Mohapatra, "Visible light communication, networking, and sensing: A survey, potential and challenges," *IEEE Commun. Surveys Tuts.*, vol. 17, no. 4, pp. 2047–2077, 4th Quart., 2015.

[11] J. Luo, L. Fan, and H. Li, "Indoor positioning systems based on visible light communication: State of the art," *IEEE Commun. Surveys Tuts.*, vol. 19, no. 4, pp. 2871–2893, 4th Quart., 2017.

[12] Y. Qiu, H.-H. Chen, and W.-X. Meng, "Channel modeling for visible light communications–A survey," *Wireless Commun. Mobile Comput.*, vol. 16, no. 14, pp. 2016–2034, Oct. 2016.

[13] A. Al-Kinani, C.-X. Wang, L. Zhou, and W. Zhang, "Optical wireless communication channel measurements and models," *IEEE Commun. Surveys Tuts.*, vol. 20, no. 3, pp. 1939–1962, 3rd Quart. 2018.

[14] D. C. O'Brien, L. Zeng, H. Le-Minh, G. Faulkner, J. W. Walewski, and S. Randel, "Visible light communications: Challenges and possibilities," in *Proc. IEEE 19th Int. Symp. Pers., Indoor Mobile Radio Commun.*, Jun. 2008, pp. 1–5.

[15] D. C. O'Brien, "Visible light communications: Challenges and potential," in *Proc. 24th Photon. Soc. Annu. Meeting*, 2011, pp. 365–366.

[16] A. Jovicic, J. Li, and T. Richardson, "Visible light communication: Opportunities, challenges and the path to market," *IEEE Commun. Mag.*, vol. 51, no. 12, pp. 26–32, Dec. 2013.

[17] *ISO/IEEE International Standard Health Informatics-Point-of-Care Medical Device Communication-Transport Profile-Infrared*, document ISO/IEEE 11073-30300:2004(E), 2004.

[18] *Safety of Laser Products—Part 1: Equipment Classification and Requirement*, document IEC 60825-1 2007.

[19] *Photo-Biological Safety of Lamps and Lamp Systems (Identical With CIE S009)*, document IEC 62471, 2006.

[20] A. Hadjidj, M. Souil, A. Bouabdallah, Y. Challal, and H. Owen, "Wireless sensor networks for rehabilitation applications: Challenges and opportunities," *J. Netw. Comput. Appl.*, vol. 36, no. 1, pp. 1–15, 2013.

[21] F. R. Gfeller and U. Bapst, "Wireless in-house data communication via diffuse infrared radiation," *Proc. IEEE*, vol. 67, no. 11, pp. 1474–1486, Nov. 1979.

[22] J. R. Barry, J. M. Kahn, W. J. Krause, E. A. Lee, and D. G. Messerschmitt, "Simulation of multipath impulse response for indoor wireless optical channels," *IEEE J. Sel. Areas Commun.*, vol. 11, no. 3, pp. 367–379, Apr. 1993.

[23] F. J. Lopez-Hermandez and M. J. Betancor, "DUSTIN: Algorithm for calculation of impulse response on IR wireless indoor channels," *Electron. Lett.*, vol. 33, no. 21, pp. 1804–1806, Oct. 1997.

[24] M. Abtahi and H. Hashemi, "Simulation of indoor propagation channel at infrared frequencies in furnished office environments," in *Proc. 6th Int. Symp. Pers., Indoor Mobile Radio Commun.*, 1995, pp. 306–310.

[25] J. B. Carruthers and P. Kannan, "Iterative site-based modeling for wireless infrared channels," *IEEE Trans. Antennas Propag.*, vol. 50, no. 5, pp. 759–765, May 2002.

[26] B. C. Jeffrey and M. K. Joseph, "Modeling of nondirected wireless infrared channels," *IEEE Trans. Commun.*, vol. 45, no. 10, pp. 1260–1268, Oct. 1997.

[27] V. Jungnickel, V. Pohl, S. Nonnig, and C. V. Helmolt, "A physical model of the wireless infrared communication channel," *IEEE J. Sel. Areas Commun.*, vol. 20, no. 3, pp. 631–640, Apr. 2002.

[28] N. Hayasaka and T. Ito, "Channel modeling of nondirected wireless infrared indoor diffuse link," *Electron. Commun. Jpn.*, vol. 90, no. 6, pp. 9–19, 2007.

[29] F. J. Lopez-Hernandez, R. Perez-Jimeniz, and A. Santamaria, "Monte Carlo calculation of impulse response on diffuse IR wireless indoor channels," *Electron. Lett.*, vol. 34, no. 12, pp. 1260–1262, Jun. 1998.

[30] F. J. López-Hernández, R. Pérez-Jiménez, and A. Santamaría, "Modified Monte Carlo scheme for high-efficiency simulation of the impulse response on diffuse IR wireless indoor channels," *Electron. Lett.*, vol. 34, no. 19, pp. 1819–1820, Sep. 1998.

[31] M. I. S. Chowdhury, W. Zhang, and M. Kavehrad, "Combined deterministic and modified Monte Carlo method for calculating impulse responses of indoor optical wireless channels," *J. Lightw. Technol.*, vol. 32, no. 18, pp. 3132–3148, Sep. 15, 2014.

[32] S. Dimitrov, R. Mesleh, H. Haas, M. Cappitelli, M. Olbert, and E. Bassow, "On the SIR of a cellular infrared optical wireless system for an aircraft," *IEEE J. Sel. Areas Commun.*, vol. 27, no. 9, pp. 1623–1638, Dec. 2009.

[33] H. Q. Nguyen, J. H. Choi, M. Kang, Z. Ghassemlooy, D. H. Kim, S. K. Lim, T. G. Kang, and C. G. Lee, "A MATLAB-based simulation program for indoor visible light communication system," in *Proc. 7th Int. Symp. Commun. Syst., Netw. Digit. Signal Process. (CSNDSP)*, 2010, pp. 537–541.

[34] S. Long, M. Khalighi, M. Wolf, S. Bourennane, and Z. Ghassemlooy, "Channel characterization for indoor visible light communications," in *Proc. 3rd Int. Workshop Opt. Wireless Commun. (IWOW)*, 2014, pp. 75–79.

[35] K. Lee, H. Park, and J. R. Barry, "Indoor channel characteristics for visible light communications," *IEEE Commun. Lett.*, vol. 15, no. 2, pp. 217–219, Feb. 2011.

[36] J. Ding and Z. Xu, "Indoor optical wireless channel characteristics with distinct source radiation patterns," *IEEE Photon. J.*, vol. 8, no. 1, pp. 1–15, Feb. 2016.

[37] H. Schulze, "Frequency-domain simulation of the indoor wireless optical communication channel," *IEEE Trans. Commun.*, vol. 64, no. 6, pp. 2551–2562, Jun. 2016.

[38] C. Chen, D. Basnayaka, and H. Haas, "Non-line-of-sight channel impulse response characterisation in visible light communications," in *Proc. IEEE Int. Conf. Commun. (ICC)*, May 2016, pp. 1–6.

[39] A. Al-Kinani, C.-X. Wang, H. Haas, and Y. Yang, "Characterization and modeling of visible light communication channels," in *Proc. IEEE 83rd Veh. Technol. Conf. (VTC Spring)*, May 2016, pp. 1–5.
[40] A. Al-Kinani, C.-X. Wang, H. Haas, and Y. Yang, "A geometry-based multiple bounce model for visible light communication channels," in *Proc. Int. Wireless Commun. Mobile Comput. Conf. (IWCMC)*, Sep. 2016, pp. 31–37.
[41] J.-H. Lee and H.-S. Lee, "A photon modeling method for characterization of indoor optical wireless system," *J. Korean Inst. Electromagn. Eng. Sci.*, vol. 19, no. 6, pp. 688–697, Jun. 2008.
[42] S. P. Rodríguez, R. P. Jiménez, B. R. Mendoza, F. J. L. Hernández, and A. J. A. Alfonso, "Simulation of impulse response for indoor visible light communications using 3D CAD models," *EURASIP J. Wireless Commun. Netw.*, vol. 2013, no. 1, pp. 1–10, Dec. 2013.
[43] F. Miramirkhani and M. Uysal, "Channel modeling and characterization for visible light communications," *IEEE Photon. J.*, vol. 7, no. 6, pp. 1–16, Dec. 2015.
[44] J. Rufo, J. Rabadan, V. Guerra, and R. Perez-Jimenez, "BRDF models for the impulse response estimation in indoor optical wireless channels," *IEEE Photon. Technol. Lett.*, vol. 29, no. 17, pp. 1431–1434, Sep. 1, 2017.
[45] M. Uysal, F. Miramirkhani, O. Narmanlioglu, T. Baykas, and E. Panayirci, "IEEE 802.15.7r1 reference channel models for visible light communications," *IEEE Commun. Mag.*, vol. 55, no. 1, pp. 212–217, Jan. 2017.
[46] F. Miramirkhani, O. Narmanlioglu, M. Uysal, and E. Panayirci, "A mobile channel model for VLC and application to adaptive system design," *IEEE Commun. Lett.*, vol. 21, no. 5, pp. 1035–1038, May 2017.
[47] F. Miramirkhani and M. Uysal, "Channel modelling for indoor visible light communications," *Phil. Trans. Roy. Soc. A, Cross-Disciplinary Challenges towards Mobile Opt. Wireless Netw.*, vol. 378, no. 2169, 2020, Art. no. 20190187.
[48] S. S. Torkestani, A. Julien-Vergonjanne, and J. P. Cances, "Mobile healthcare monitoring in hospital based on diffuse optical wireless technology," in *Proc. 21st Annu. Int. Symp. Pers., Indoor Mobile Radio Commun.*, 2010, pp. 1055–1059.
[49] S. S. Torkestani, N. Barbot, S. Sahuguede, A. Julien-Vergonjanne, and J. P. Cances, "Performance and transmission power bound analysis for optical wireless based mobile healthcare applications," in *Proc. IEEE 22nd Int. Symp. Pers., Indoor Mobile Radio Commun.*, Dec. 2011, pp. 2198–2202.
[50] S. S. Torkestani, A. Julien-Vergonjanne, and J. P. Cances, "Indoor optical wireless system dedicated to healthcare application in hospital," in *Proc. 7th Int. Symp. Commun. Syst., Netw. Digit. Signal Process.*, 2010, pp. 542–546.
[51] S. S. Torkestani, S. Sahuguede, A. Julien-Vergonjanne, J. Cances, and J. C. Daviet, "Infrared communication technology applied to indoor mobile healthcare monitoring system," *Int. J. E-Health Med. Commun.*, vol. 3, no. 3, pp. 1–11, Jul. 2012.
[52] E. A. Alyan and S. A. Aljunid, "Development of wireless optical CDMA system for biosignal monitoring," *Optik*, vol. 145, pp. 250–257, Sep. 2017.
[53] A. M. Khalid, G. Cossu, and E. Ciaramella, "Diffuse IR-optical wireless system demonstration for mobile patient monitoring in hospitals," in *Proc. 15th Int. Conf. Transparent Opt. Netw. (ICTON)*, Jun. 2013, pp. 1–4.
[54] P. Toumieux, L. Chevalier, S. Sahuguède, and A. Julien-Vergonjanne, "Optical wireless connected objects for healthcare," *Healthcare Technol. Lett.*, vol. 2, no. 5, pp. 118–122, 2015.
[55] C. Le Bas, L. Chevalier, P. Toumieux, S. Sahuguede, and A. Julien-Vergonjanne, "Experimental study of an optical wireless physical activity monitoring system," in *Proc. 10th Int. Symp. Med. Inf. Commun. Technol. (ISMICT)*, Mar. 2016, pp. 1–5.
[56] T. B. Hoang, S. Sahuguede, and A. Julien-Vergonjanne, "Behavior of non-directed optical wireless channel considering receiver orientation," in *Proc. 20th Int. Symp. Wireless Pers. Multimedia Commun. (WPMC)*, Dec. 2017, pp. 223–228.
[57] T. B. Hoang, S. Kandukuri, S. Sahuguede, and A. Julien-Vergonjanne, "Infrared mobile transmissions for smart indoor applications," in *Proc. 11st Int. Symp. Commun. Syst., Netw. Digit. Signal Process. (CSNDSP)*, Jul. 2018, pp. 1–6.
[58] A. Kaba, S. Sahuguede, and A. Julien-Vergonjanne, "Channel modeling of an optical wireless body sensor network for walk monitoring of elderly," *Sensors*, vol. 21, no. 9, pp. 1–19, 2021.
[59] Y.-K. Cheong, X.-W. Ng, and W.-Y. Chung, "Hazardless biomedical sensing data transmission using VLC," *IEEE Sensors J.*, vol. 13, no. 9, pp. 3347–3348, Sep. 2013.
[60] C. L. Bas, S. Sahuguede, A. Julien-Vergonjanne, A. Behlouli, P. Combeau, and L. Aveneau, "Impact of receiver orientation and position on visible light communication link performance," in *2015 4th Int. Workshop Opt. Wireless Commun. (IWOW)*, 2015, pp. 1–5.
[61] C. Le Bas, S. Sahuguede, A. Julien-Vergonjanne, A. Behlouli, P. Combeau, and L. Aveneau, "Human body impact on mobile visible light communication link," in *Proc. 10th Int. Symp. Commun. Syst., Netw. Digit. Signal Process. (CSNDSP)*, Jul. 2016, pp. 1–6.
[62] A. Behlouli, P. Combeau, S. Sahuguède, A. Julien-Vergonjanne, C. L. Bas, and L. Aveneau, "Impact of physical and geometrical parameters on visible light communication links," in *Proc. Adv. Wireless Opt. Commun. (RTUWO)*, 2017, pp. 73–76.
[63] C. Le Bas, T. B. Hoang, S. Sahuguede, and A. Julien-Vergonjanne, "Lighting fixture communicating in infrared and visible for indoor health monitoring," in *Proc. IEEE 19th Int. Conf. E-Health Netw., Appl. Services (Healthcom)*, Oct. 2017, pp. 1–6.
[64] C. Lebas, S. Sahuguede, A. Julien-Vergonjanne, P. Combeau, and L. Aveneau, "Infrared and visible links for medical body sensor networks," in *Proc. Global LIFI Congr. (GLC)*, vol. 2018, pp. 1–6.
[65] T. B. Hoang, S. Sahuguede, and A. Julien-Vergonjanne, "Optical wireless network design for off-body-sensor based monitoring," *Wireless Commun. Mobile Comput.*, vol. 2019, pp. 1–13, Sep. 2019.
[66] A. A. Farid and S. Hranilovic, "Outage capacity optimization for free-space optical links with pointing errors," *J. Lightw. Technol.*, vol. 25, no. 7, pp. 1702–1710, Jul. 1, 2007.
[67] L. Chevalier, S. Sahuguede, A. Julien-Vergonjanne, P. Combeau, and L. Aveneau, "Investigation of wireless optical technology for communication between on-body nodes," in *Proc. 2nd Int. Workshop Opt. Wireless Commun. (IWOW)*, 2013, pp. 79–83.
[68] L. Chevalier, S. Sahuguede, and A. Julien-Vergonjanne, "Investigation of obstacle effect on wireless optical on-body communication performance," in *Proc. 21st Int. Conf. Telecommun. (ICT)*, May 2014, pp. 103–107.
[69] L. Chevalier, S. Sahuguede, and A. Julien-Vergonjanne, "Performance evaluation of wireless optical communication for mobile BAN scenario with blocking effects," in *Proc. 9th Int. Symp. Commun. Syst., Netw. Digit. Sign (CSNDSP)*, Jul. 2014, pp. 319–324.
[70] L. Chevalier, S. Sahuguede, and A. Julien-Vergonjanne, "Wireless optical technology based body area network for health monitoring application," in *Proc. IEEE Int. Conf. Commun. (ICC)*, Jun. 2015, pp. 2863–2868.
[71] O. Haddad, M.-A. Khalighi, S. Zvanovec, and M. Adel, "Channel characterization and modeling for optical wireless body-area networks," *IEEE Open J. Commun. Soc.*, vol. 1, pp. 760–776, 2020.
[72] W. Noonpakdee, "Performance analysis of passive—Active optical wireless transmission for personal health monitoring," in *Proc. 6th Int. Conf. Ubiquitous Future Netw. (ICUFN)*, Jul. 2014, pp. 17–21.
[73] Y. Y. Tan and W.-Y. Chung, "Mobile health-monitoring system through visible light communication," *Bio-Med. Mater. Eng.*, vol. 24, no. 6, pp. 3529–3538, Sep. 2014.
[74] W. A. Cahyadi, T.-I. Jeong, Y.-H. Kim, Y.-H. Chung, and T. Adiono, "Patient monitoring using visible light uplink data transmission," in *Proc. Int. Symp. Intell. Signal Process. Commun. Syst. (ISPACS)*, Nov. 2015, pp. 431–434.
[75] V. P. Rachim, J. An, P. N. Quan, and W. Chung, "A novel smartphone camera-LED communication for clinical signal transmission in mhealth-rehabilitation system," in *Proc. 39th Annu. Int. Conf. Eng. Med. Biol. Soc. (EMBC)*, 2017, pp. 3437–3440.
[76] R. Liang, *Optical Design for Biomedical Imaging*, 1st ed. Bellingham, WA, USA: SPIE, 2010.
[77] C. R. Simpson, M. Kohl, M. Essenpreis, and M. Cope, "Near-infrared optical properties ofex vivohuman skin and subcutaneous tissues measured using the Monte Carlo inversion technique," *Phys. Med. Biol.*, vol. 43, no. 9, pp. 2465–2478, Sep. 1998.
[78] D. M. Ackermann, B. Smith, X.-F. Wang, K. L. Kilgore, and P. H. Peckham, "Designing the optical interface of a transcutaneous optical telemetry link," *IEEE Trans. Biomed. Eng.*, vol. 55, no. 4, pp. 1365–1373, Apr. 2008.
[79] W. A. G. Bruls and J. C. Van Der Leun, "Forward scattering properties of human epidermal layers," *Photochem. Photobiol.*, vol. 40, no. 2, pp. 231–242, Aug. 1984.
[80] T. Lister, P. A. Wright, and P. H. Chappell, "Optical properties of human skin," *J. Biomed. Opt.*, vol. 17, no. 9, 2012, Art. no. 90901.
[81] T. Maeda, N. Arakawa, M. Takahashi, and Y. Aizu, "Monte Carlo simulation of spectral reflectance using a multilayered skin tissue model," *Opt. Rev.*, vol. 17, no. 3, pp. 223–229, May 2010.

[82] I. V. Meglinski and S. J. Matcher, "Quantitative assessment of skin layers absorption and skin reflectance spectra simulation in the visible and near-infrared spectral regions," *Physiol. Meas.*, vol. 23, no. 4, pp. 741–753, Nov. 2002.
[83] G. Appelboom, E. Camacho, M. E. Abraham, S. S. Bruce, E. L. Dumont, B. E. Zacharia, R. D'Amico, J. Slomian, J. Y. Reginster, O. Bruyère, and E. S. Connolly, "Smart wearable body sensors for patient self-assessment and monitoring," *Arch. Public Health*, vol. 72, no. 1, p. 28, Dec. 2014.
[84] V. Dremin, E. Zherebtsov, A. Bykov, A. Popov, A. Doronin, and I. Meglinski, "Influence of blood pulsation on diagnostic vol. in, pulse oximetry and photoplethysmography measurements," *Appl. Opt.*, vol. 58, no. 34, pp. 9398–9405, 2019.
[85] F. P. Bolin, L. E. Preuss, R. C. Taylor, and R. J. Ference, "Refractive index of some mammalian tissues using a fiber optic cladding method," *Appl. Opt.*, vol. 28, no. 12, pp. 2297–2303, Jun. 1989.
[86] F. Miramirkhani and M. Uysal, "Visible light communication channel modeling for underwater environments with blocking and shadowing," *IEEE Access*, vol. 6, pp. 1082–1090, 2017.
[87] Facility Guidelines Institute. (2020). *Interim Amendment for the 2018 Residential Guidelines*. [Online]. Available: https://fgiguidelines.org/wp-content/uploads/2020/08/FGI-2018-RES-Interim-Amendment-ResidentRooms_2020-08-28.pdf
[88] State of Kuwait Ministry of Health Infection Control Directorte. (2008). *Guidelines for general ward design*. [Online]. Available: http://www.icdkwt.com/pdf/policiesandguidelines/DesignandConstruction/GuidelinesforGeneralWardDesign-2008.pdf
[89] *Lighting for Hospitals and Healthcare Facilities*, Illuminating engineering society (IES) of North America, New York, NY, USA, 2016.
[90] T. Komine, J. H. Lee, S. Haruyama, and M. Nakagawa, "Adaptive equalization system for visible light wireless communication utilizing multiple white LED lighting equipment," *IEEE Trans. Wireless Commun.*, vol. 8, no. 6, pp. 2892–2900, Jun. 2009.
[91] R. Mitra, G. Kaddoum, and V. Bhatia, "Hyperparameter-free transmit-nonlinearity mitigation using a kernel-width sampling technique," *IEEE Trans. Commun.*, vol. 69, no. 4, pp. 2613–2627, Apr. 2021.
[92] E. Sfeir, R. Mitra, G. Kaddoum, and V. Bhatia, "RFF based detection for SCMA in presence of PA nonlinearity," *IEEE Commun. Lett.*, vol. 24, no. 11, pp. 2604–2608, Nov. 2020.
[93] E. Sfeir, R. Mitra, G. Kaddoum, and V. Bhatia, "Performance analysis of maximum-correntropy based detection for SCMA," *IEEE Commun. Lett.*, vol. 25, no. 4, pp. 1114–1118, Apr. 2021.
[94] R. Mitra, F. Miramirkhani, and V. Bhatia, "Low complexity least minimum symbol error rate based post-distortion for vehicular VLC," *IEEE Trans. Veh. Technol.*, vol. 69, no. 10, pp. 11800–11810, Oct. 2020.
[95] R. Mitra, S. Jain, and V. Bhatia, "Least minimum symbol error rate based post-distortion for VLC using random Fourier features," *IEEE Commun. Lett.*, vol. 24, no. 4, pp. 830–834, Apr. 2020.
[96] R. Mitra, G. Kaddoum, G. Dahman, and G. Poitau, "Error analysis of localization based on minimum-error entropy with fiducial points," *IEEE Commun. Lett.*, vol. 25, no. 4, pp. 1187–1191, Apr. 2021.

BARIS DONMEZ (Member, IEEE) is currently pursuing the M.Sc. degree with the OPTWiCOM Research Group, Isik University, Istanbul, Turkey, under the supervision of Dr. Farshad Miramirkhani. He joined the OPTWiCOM Research Group as a Research Assistant, in 2020. His current research interests include VLC-based medical body sensor networks and channel modeling.

RANGEET MITRA (Member, IEEE) received the Ph.D. degree from IIT Indore, in 2017. He currently works with the Ecole De Technologie Superieure, Montreal, Canada, as a Postdoctoral Researcher. He has published several articles in adaptive signal processing in RKHS and nonlinear signal processing. His research interests include adaptive signal processing, reproducing kernel Hilbert spaces, information-theoretic learning, deep learning, and their analysis/applications for various next-generation communication systems.

FARSHAD MIRAMIRKHANI (Member, IEEE) received the B.Sc. and M.Sc. degrees in electrical and electronics, and communication engineering from the University of Isfahan, Isfahan, Iran, in 2011 and 2014, respectively, and the Ph.D. degree in electrical and electronics engineering from Ozyegin University, Istanbul, Turkey, in 2018. He is currently an Assistant Professor with the Department of Electrical and Electronics Engineering, Isik University. He has also contributed to the standardization works of IEEE 802.15.13 (Short Range Optical Wireless Communications) and IEEE 802.11bb (Light Communications for Wireless Local Area Networking). The LiFi channels developed by him were selected as the LiFi Reference Channel Models by the IEEE 802.15.13 and IEEE 802.11bb Task Groups. His current research interests include optical wireless communications, VLC-based medical body sensor networks, indoor visible light communications, vehicular visible light communications, underwater visible light communications, and channel modeling. He also serves as a Telecommunications Advisory Board Member for Cambridge Scholars Publishing, an Academic Editor for IntechOpen, and an Editorial Board Member of Wireless Communications for *Frontiers in Communications and Networks*.